Georgia Institute of Technology
Atlanta, Georgia 30332

ACTIVELY CONTROLLED SHAFT SEALS

FOR AEROSPACE APPLICATIONS

Semiannual Status Report, July - December, 1991

NASA Research Grant NAG 3-974

Principal Investigator: Richard F. Salant
Research Assistant: Paul Wolff
Designer: Samuel Navon
College of Engineering
School of Mechanical Engineering

E25-666

TABLE OF CONTENTS

iv

LIST OF TABLES

LIST OF FIGURES

Page

LIST OF SYMBOLS

General Notation

A_{face} area of seal face

c   elasticity coefficient (N/m^2)

D   electric flux

d   piezoelectric coefficient (strain/electric field)

e   piezoelectric coefficient (stress/electric field)

F_{close} closing force

F_{open} opening force

F_{spring} spring force

G   gravitational acceleration

H   convective heat transfer coefficient

h   film thickness

k   thermal conductivity

l_G gap width

m   mass flow rate

N_b balance ratio

Nu   Nusselt Number

P   pressure

P^* nondimensional pressure $(P^2-P_i^2)/(P_o^2-P_i^2)$

Q   heat generation rate

q   heat generation rate per unit volume

r   radial coordinate

r_b balance radius

r^* nondimensional radial coordinate (r/r_i)

R universal gas constant

Re Reynold's Number

S strain

s elasticity coefficient (m^2/N)

T temperature

t time

V_r radial velocity

V_z axial velocity

V_θ circumferential velocity

z axial coordinate

Greek Letters

α coefficient of thermal expansion

α^* radius ratio of seal faces $r_i/(r_o-r_i)$

β slope of seal face

δ coning

δ^* nondimensional coning (δ/h_i)

ϵ dielectric coefficient

ζ dissipation factor

θ circumferential coordinate

κ relaxation factor

μ viscosity

ν kinematic viscosity

ρ density

τ stress

ω rotational speed

Subscripts

i   value at inner radius of seal interface
           new value from new iteration

o   value at outer radius of seal interface
           old value from previous iteration

r   radial direction

z   axial direction

θ circumferential direction

SUMMARY

Actively controlled mechanical seals have recently been developed for industrial use. This study investigates the feasibility of using such seals for aerospace applications.

In a noncontacting mechanical seal, the film thickness depends on the geometry of the seal interface. The amount of coning, which is a measure of the radial convergence or divergence of the seal interface, has a primary effect on the film thickness. Active control of the film thickness is established by controlling the coning with a piezoelectric material.

A mathematical model has been formulated to predict the performance of an actively controlled mechanical seal. A pressure distribution in the seal interface is first determined through an analytic solution of The Navier-Stokes Equations. The viscous heat generation rate in the seal interface is then computed based on an initial guess of the film thickness. The amount of coning due to pressure, thermal, and voltage deformations is computed with finite element techniques, and a modified film thickness is calculated. This procedure is repeated until the film thickness converges.

Based on results from this model, a design of an actively controlled mechanical seal has been developed for use in a liquid oxygen turbopump. This seal has been built and testing is now underway.

CHAPTER I

INTRODUCTION

Mechanical seals, also known as face seals, are commonly used in turbomachinery where rotating shaft seals are required. Figure 1 presents a typical mechanical seal. These seals generally consist of a rotating element (also called the rotor), a nonrotating element (also called the stator), a spring, and secondary seals. One of the elements, known as the floating element, is mounted on springs and dynamically tracks the face of the other element. In Figure 1, the floating element is the stator.

The operation of a mechanical seal can be understood by examining Figure 1. Two leakage paths from the outside pressure to the lower, inside pressure can be seen in Figure 1: the gap between the housing and the floating component, and the gap between the floating component and the rotor. Leakage through the first path is prevented by the secondary seal. The second leakage path is restricted by the spring and pressure forces which act on the floating component to push it against the rotor. Extremely low leakage rates occur for typical operation of a well designed face seal.

1

Face seals are generally classified as either contacting or noncontacting. In a contacting seal the faces touch, resulting in high surface temperatures, high contact stresses, and high wear rates. This is in contrast to noncontacting face seals which operate with a thin lubricating film between the seal faces. This film prevents wear and ensures a longer seal life. For applications where reliability is a principle concern, noncontacting seals are preferred.

Noncontacting face seals are further classified as either hydrostatic or hydrodynamic. In a hydrostatic face seal, the pressure distribution within the lubricating film is independent of the rotational speed of the rotor. This type of operation occurs for seals whose faces are flat and axisymmetric. The operation of a hydrodynamic seal, on the other hand, depends on the rotational speed of the shaft. These seals typically have non-axisymmetric geometries, such as spiral grooves or steps, machined or etched into one of the seal faces. Elevated pressures are generated within the lubricating film due to the rotation of the seal rotor.

The seal of interest in the present study is a hydrostatic face seal. The pressure distribution within the lubricating film of such a seal is strongly dependent on the radial convergence of the seal faces. This radial convergence is known as coning and is shown in Figure 1. The coning is

2

considered positive when the faces of the seal converge in the radial direction from high to low pressure. For a seal with positive coning (required for stable seal operation), the average pressure within the film increases with either an increase in coning or a decrease in film thickness.

The thickness of the lubricating film is determined by the forces acting on the floating component of the seal. These forces are presented in Figure 2, which shows the floating component of the seal that was designed for the present study. The closing force tends to push the faces of the seal together and is a function of the balance ratio of the seal, the sealed pressure, the face area, and the spring force. The balance ratio is a geometric parameter (see Chapter IV - Mathematical Model, Equation 3). The opening force tends to push the faces of the seal apart and is produced by the pressure distribution within the lubricating film. The opening force increases as the coning increases or the film thickness decreases. A well designed seal operates so that the closing and opening forces balance with a film thickness on the order of a few microns (2-4 um). An increase in coning will result in an increase in film thickness; conversely, a decrease in coning will result in a decrease in film thickness.

The coning in a face seal is typically a result of mechanical and thermal deformations. A recent approach however, employed in industrial seals, utilizes a

3

piezoelectric material to actively control the coning [Salant et. al., 1987; Salant et. al., 1989]. Figure 3 presents a sketch of the actively controlled seal configuration. The seal consists of a piezoelectric actuator, thermocouples embedded in a face of the seal, and a microcomputer based control system.

The seal configuration is such that when voltage is applied to the piezoelectric actuator, the latter produces positive coning of the nonrotating face. Typical operation of this seal involves applying a large initial voltage to the piezoelectric element which produces a relatively large film thickness. As the voltage is decreased, the faces approach a contact condition which causes a sharp rise in the temperature of the seal faces. This temperature increase is measured by the thermocouples embedded in a face of the seal. A slight increase in voltage then prevents face contact while producing an optimal film thickness. This control scheme continuously minimizes film thickness but prevents excessive face contact, which results in reduced leakage and increased reliability.

The goal of the present project is to develop an actively controlled aerospace face seal for a liquid oxygen (LOX) turbopump (see Figure 4) which will be used in an orbital transfer vehicle. Currently, floating ring seals are utilized for the helium buffer seal in the liquid oxygen turbopump (see Figure 5). As can be seen in Figure 5, helium is used as a

4

buffer gas to prevent contact between the hot gases which drive the turbine, and the liquid oxygen. The floating ring seals operate with a clearance on the order of 20 um which is 5 times larger than a representative operating clearance for a conventional face seal (4 um). The leakage in a seal is proportional to the clearance cubed; therefore a reduction in clearance by a factor of 5 reduces the leakage by a factor of 125. This reduction in leakage (and reduction in stored helium) represents considerable savings for an aerospace mission in which payload is a principle concern. Therefore, it is desired to replace the floating ring seals with face seals.

Although conventional face seals operate with much lower leakage rates than floating ring seals, they are generally not as reliable as floating ring seals, and therefore have not previously been used in the helium purge assembly. Face seals could inadvertently operate in a contacting mode, resulting in face damage and high face temperatures, the latter increasing the risk of explosion. Conversely, if the film thickness becomes excessive, large leakage rates result which could deplete the supply of the helium purge gas. The controllable seal would be more reliable than a conventional face seal because the film thickness could be continuously optimized. Such a seal could therefore be used in a LOX turbopump.

This thesis presents the design and analysis of an actively controlled seal. The design of the electronic control system however, was considered beyond the scope of this thesis, and is therefore not included. Figure 6 presents the configuration of the seal. This is a tandem seal configuration with one rotating face and two floating elements. The control components for this seal consist of the deformable face assembly, thermocouples embedded in the deformable face assembly, a voltage supply, and a controller. The principle of operation of this seal is similar to that of the actively controlled seal previously described.

The analysis of this seal was performed with a mathematical model containing an iterative procedure. The film thickness of the seal is dependent on the coning of the seal, which is produced by thermal-, pressure-, and voltage-induced deformations. However, the thermal deformations are dependent on viscous heat generation within the gas film which is a function of the film thickness. Therefore, an iterative procedure was necessary to compute the film thickness.

The first part of the iterative procedure involved computing the pressure distribution within the lubricating film from an analytic solution of the governing fluid mechanics equations. The viscous heat generation rate within the lubricating film was then computed utilizing an initial guess of the film thickness. Based on this viscous heat

generation rate and the thermal boundary conditions, temperatures of the seal components were computed with the finite element method. The thermal, pressure and voltage loads acting on the seal components resulted in a coning deformation of the seal faces which was also computed with the finite element method. A new film thickness, which resulted from the coning deformation, was computed by performing a force balance on the floating component of the seal. The modified film thickness changed the viscous heat generation within the lubricating film, which in turn changed the temperature profiles of the seal and modified the coning deformation of the seal faces. This procedure was repeated until the film thickness and temperatures of the seal components converged to a stationary value.

Film thickness and leakage rates of various seal designs as a function of voltage applied to the piezoelectric element were computed with this mathematical model. The performance of the seal under different thermal and pressure boundary conditions was also evaluated with this model.

The design and analysis of the actively controlled face seal presented in this thesis represent the first phase of the seal development. The second phase will involve fabrication of the seal and testing in a laboratory test rig which operates at room temperature (294 K). The final phase will

involve modifying the design for further testing and eventual use in a LOX turbopump.

CHAPTER II

LITERATURE REVIEW

Basis of Mathematical Model

The mathematical model presented in this thesis is based on the assumptions that there is a thin fluid film between the seal faces and that the load support is primarily due to the hydrostatic pressure distribution. These assumptions however, are not immediately apparent. For many years it was believed that all seals operated in a contacting mode [Mayer, 1977] and the load was carried by the mechanical contact between the seal faces. It is not surprising that the operation of mechanical seals was not well understood, since it is now known that the film between the faces of a noncontacting seal is on the order of a few microns thick. Experimental validation of any assumptions is therefore extremely difficult. In recent years however, a much better understanding of mechanical seals has been achieved through extensive research.

Existence of Film

The assumption that a thin fluid film exists between the faces of a mechanical seal has been long suspected [Nau, 1967]

and recently directly validated through an experiment. Doust and Parmar [1985] successfully measured fluid film profiles between the faces of a mechanical seal to determine the effects of pressure and thermal loads on the deformation of the seal faces. In their investigation, they instrumented a mechanical seal with capacitance probes to measure film thickness. These experiments were performed for sealed pressures between 0 and 4 MPa, for various face temperatures, and for shaft speeds up to 3000 rpm. This study clearly indicated that a fluid film existed for the operating conditions examined.

Salant and Key [1984] also verified that a fluid film existed by examining the torque variations of a seal as a function of speed and load, and by measuring the wear rate of a carbon-graphite seal face. They then compared these results with known characteristics of continuous film and boundary lubrication regimes, thereby verifying the existence of a continuous film.

Load Support

Another assumption of the present study is that for a seal with flat axisymmetric faces, the opening force is produced only by the hydrostatic pressure distribution. This assumption was verified by Salant and Key [1984], who compared the forces generated by the hydrostatic pressure distribution

to the forces generated from hydrodynamic effects. The conditions studied for the hydrodynamic effects included roughness, waviness, misalignment, and eccentricity of the seal faces. They computed the opening forces from the hydrodynamic effects based on equations which were developed by previous researchers. These results showed that for axisymmetric, noncontacting face seals, the hydrodynamic effects can be ignored relative to the opening force generated by the hydrostatic pressure distribution.

Previous Seal Models

Mathematical models have been created in recent years which give meaningful predictions of the performance of mechanical seals. This is a significant achievement considering that the film thickness is on the order of microns and deformations on the order of microns affect the performance of the seal. Useful models must therefore predict these extremely small deformations. The mathematical models which concern this project most directly are those created by Metcalf [1971, 1979, 1981], and Salant and Key [1984].

The model utilized for the analysis of the actively controlled seal is essentially based on the research of Metcalf. Metcalf [1971] utilized a hydrostatic model to predict pressure distributions, leakage rates, and viscous heat generation within the fluid film of a mechanical seal.

This model demonstrated that the hydrostatic pressure distribution is strongly dependent on the profile of the fluid film. He then utilized finite element techniques to compute the deformations of the seal faces from which the film profile could be determined [Metcalf, 1979]. The deformations were produced by pressure loads, and by loads due to the interfacial friction between the two component assemblies. A series of experiments were then performed on various seal assemblies to validate these models [Metcalf, 1981]. Leakage rates were measured, from which the deformations of the seal faces were computed. These experimentally determined deformations correlated well with those obtained from the analytical models.

The results of Metcalf were extended and further validated by Salant and Key [1984], who included the effects of thermal deformations. Several seals were tested, and their performance was compared to the results predicted by the analytical model. It was found that the analytical model predictions correlated well with the observed behavior of the seals.

Actively Controlled Seals

The film thickness in a mechanical seal is determined by the opening and closing forces which act on the floating component of the seal. Previous researchers have examined

various strategies to control the forces which act on the seal, and thereby control the film thickness.

As previously discussed (see Chapter I - Introduction), the opening force is strongly dependent on the coning of the seal faces. Salant et. al. [1987] investigated a controllable seal which controlled the opening force of the seal by adjusting the coning of the seal faces. The coning in this seal was produced by a stack of piezoelectric elements which were located near the inner radius of the nonrotating seal face. A voltage applied to the piezoelectric elements caused them to expand in the axial direction and also pushed the inside radius of the seal face in the axial direction. Since the outer radius of the seal face was restrained, a coning deformation was thereby produced, which increased as the voltage was increased. In addition to the piezoelectric elements, the control components for this seal consisted of a thermocouple embedded in the nonrotating seal face, a thermocouple in the seal cavity to monitor the temperature of the sealed fluid, a voltage supply, and a microprocessor-based control system.

The control strategy for this seal was based on establishing a reference point where face contact occurred. A slight increase in voltage then prevented face contact while the film thickness was minimized. The reference point where contact occurred was identified in one of two ways, by either

measuring a large temperature difference between the seal face and seal chamber, or by detecting oscillations in the seal face temperature. Large temperature differences would occur for face contact due to the heat generation produced by friction between the seal faces. Temperature oscillations were also an indication of zero film thickness because thermoelastic instabilities have been found to occur when seal faces contact. Once a minimum film thickness was found, the voltage was held constant until the temperature difference between the seal face and the seal chamber changed by more than some preset limits. If this occurred, the control system once again searched for an optimum film thickness. Heilala and Kangasniemi [1987] also designed a seal with a controllable opening force. This was achieved with a control system which consisted of a compressed air supply and supply line to the seal film, a thermocouple embedded in the face of the nonrotating component, a pneumatic valve, and a controller. The input to the control system was the temperature of the seal face, measured by the thermocouple, which gave an indication of the film thickness. As the face temperature increased, the controller opened the pneumatic valve which increased the amount of compressed air fed into the seal film. The compressed air increased the pressure within the seal film, and thereby increased the opening force, which increased the film thickness. Results from this

14

experiment demonstrated that lower face temperatures were achieved for the controllable seal as compared to an uncontrolled seal.

Etsion [1990] investigated a controllable hydrodynamic seal which was based on a variable closing force. The control system was similar to the control system utilized by Heilala and Kangasniemi, however the compressed air was supplied to the backside of the floating component. The input for this control system was also the face temperature of seal which was read by a microcomputer. Based on the face temperature, a back pressure was computed by the microcontroller, and the electro-pneumatic valve was then adjusted by the microcontroller to produce the desired back pressure.

Etsion investigated the response of this seal to changes in the speed of the test rig. Both a linear and nonlinear control algorithm were utilized to compute the back pressure as a function of the face temperature of the seal. These control algorithms enabled the control system to track the set point temperature reasonably well, however the nonlinear control algorithm demonstrated a faster response time.

CHAPTER III

DESIGN CONSIDERATIONS

Current Helium Purge Seal

Figure 4 presents a diagram of a typical turbopump (not the one of the present study). Hot gases enter on one side and drive the turbine rotor of the turbopump. This causes the pump impeller on the opposing side of the turbopump to rotate, thereby pumping the LOX (liquid oxygen). If the hot gases come in contact with the LOX, components of the turbine could ignite and a catastrophic explosion would result. Contact between the LOX and hot gases is prevented with a series of seals which includes the helium purge assembly, presented in Figure 5. The helium purge assembly introduces pressurized helium near the midpoint of the turbopump. The helium flows axially outward, away from the helium purge assembly, and toward both the turbine rotor and the pump impeller. This prevents contact between the hot gases and LOX.

Description of Proposed Design

Current LOX turbopump designs utilize double floating ring seals in the helium purge assembly, as shown in Figure 5. The major objective in replacing these ring seals with face seals

16

is to reduce helium leakage while ensuring that no contact occurs between the LOX and hot gases. To accomplish this, a tandem seal configuration was chosen which is presented in Figure 6. The components for this configuration include one rotating face and two nonrotating floating components. The rotating face is attached to the shaft with an interference fit and has an elastomeric O-ring located at its inner radius. Each nonrotating component consists of a holder, a deformable face assembly, a spring, and two secondary seals.

The operation of this seal can be understood by examining Figure 6 and considering the leakage path between the LOX and hot gases. The configuration of the seal constrains the gases to flow through the seal cavity for contact between the LOX and hot gases to occur. However, the seal cavity contains pressurized helium which prevents the lower pressure hot gases and oxygen from entering. Helium leakage from the seal cavity is minimized by controlling the film thickness between the faces of the seal with the active control system. Contact between the seal faces is also minimized by the active control system.

The operating procedure for the seal will consist of the following steps: pressurizing the helium purge assembly, applying voltage to the piezoelectric element to ensure a large film thickness, starting the turbopump, and minimizing the film thickness with the active control system once the

17

turbopump reaches steady state operation. Pressurizing the helium purge assembly provides the opening force for the seal and is necessary to separate the seal faces. Once the seal cavity is pressurized, a voltage applied to the piezoelectric element will produce positive coning which establishes an initial film thickness. The initial film thickness should be relatively large to prevent contact between the seal faces during transient startup conditions. Once the turbopump is started and steady state operation is reached, the active control system will minimize the film thickness by continually reducing the voltage applied to the piezoelectric element. The thermocouples embedded in the face of the floating component of the seal will detect an increase in temperature as the seal faces approach a contact condition. A slight increase in voltage will then prevent contact of the seal faces while ensuring a minimum film thickness. Any subsequent changes in film thickness will be detected by the thermocouples, and corrected by the control system. The control system will be operated by a microcomputer.

Design Constraints

The size and operating conditions of a LOX turbopump impose severe constraints on the design of a face seal for the helium purge assembly. Design constraints for this seal are presented in Figure 7. The size of the seal envelope is 3.81

18

cm (1.5 in) in the axial direction and 1.27 cm (0.5 in) from the outside radius of the shaft to the outside radius of the envelope. This seal envelope is considerably smaller than the size required for current commercially available tandem seal configurations. The high and low pressure sides of the seal are at 1.38 x 10^6 Pa (200 psi) and 1.1 x 10^5 Pa (15.9 psi), respectively. Temperatures which affect the design of the seal include the temperature of the hot gas and helium drain (469 K, 385 F), the temperature of the LOX and helium drain (123 K, -238 F), and the temperature of the helium at the high pressure side (294 K, 70 F). The thermal deformations produced by these temperature gradients have a significant effect on the coning deformations of the seal faces and thereby influence the performance of the seal. The shaft of the turbopump operates at a speed of 7,330 rad/sec (70,000 rpm).

CHAPTER IV

MATHEMATICAL MODEL

A mathematical model was used to evaluate different seal designs and the effects of the various boundary conditions on the performance of the seal. The primary performance parameters of concern were the film thickness and leakage rate as functions of the voltage applied to the piezoelectric element.

Description of Force Balance

To compute the film thickness and leakage rate for a mechanical seal under steady state conditions, it is first necessary to perform a force balance between the opening and closing forces acting on the floating component of the seal. Figure 2 presents the floating component of the proposed seal design and the forces which act upon it. The opening force tends to push the faces apart and consists of the pressure forces in the gas film acting on the seal face. The closing force tends to push the faces of the seal together and is due to the pressure of the sealed fluid acting on the back side of the holder and the spring force. The closing force is given by,

$$F_{close} = A_{face} * (N_b * (P_o - P_i) + P_i) + F_{spring} \qquad (1)$$

and the opening force is computed from,

$$F_{open} = \int_{A_{face}} P dA \qquad (2)$$

The closing force depends on the balance ratio which is defined by the following equation,

$$N_b = \frac{r_o^2 - r_b^2}{r_o^2 - r_i^2} \qquad (3)$$

The balance ratio represents a ratio of two areas: the area of the backside of the floating component over which the pressure which tends to close the seal acts, to the area on the frontside of the floating component over which the film pressure which tends to open the seal acts.

The closing force depends on the balance ratio, pressure within the seal cavity, and the spring force. Once these quantities are specified, it is straightforward to compute the closing force which then remains constant. However to compute the opening force, it is necessary to determine the pressure

distribution within the gas film, which requires solution of the governing fluid mechanics equations.

Fluid Mechanics Model of the Gas Film

Pressure Distribution and Seal Leakage

The pressure within the gas film generates the opening force and also causes deformations of the seal faces which affect the coning. Therefore, it is essential to compute the pressure distribution to predict the performance of a mechanical seal. The pressure distribution is governed by the Navier-Stokes Equations which are given below in cylindrical coordinates;

$$\rho \left(\frac{\partial V_r}{\partial t} + V_r \frac{\partial V_r}{\partial r} + \frac{V_\theta}{r} \frac{\partial V_r}{\partial \theta} - \frac{V_\theta^2}{r} + V_z \frac{\partial V_r}{\partial z} \right) = \mu \left(\frac{\partial}{\partial r} \left(\frac{1}{r} \frac{\partial (r V_r)}{\partial r} \right) + \frac{1}{r^2} \frac{\partial^2 V_r}{\partial \theta^2} + \frac{\partial^2 V_r}{\partial z^2} - \frac{2}{r^2} \frac{\partial V_\theta}{\partial \theta} \right) - \frac{\partial P}{\partial r} + \rho G_r \tag{4}$$

$$\rho \left(\frac{\partial V_\theta}{\partial t} + V_r \frac{\partial V_\theta}{\partial r} + \frac{V_\theta}{r} \frac{\partial V_\theta}{\partial \theta} + V_r \frac{V_\theta}{r} + V_z \frac{\partial V_\theta}{\partial z} = \mu \left(\frac{\partial}{\partial r} \left(\frac{1}{r} \frac{\partial (r V_\theta)}{\partial r} \right) + \frac{1}{r^2} \frac{\partial^2 V_\theta}{\partial \theta^2} + \frac{\partial^2 V_\theta}{\partial z^2} + \frac{2}{r^2} \frac{\partial V_r}{\partial \theta} \right) - \frac{1}{r} \frac{\partial P}{\partial \theta} + \rho G_\theta \tag{5}$$

22

$$\rho \left(\frac{\partial V_z}{\partial t} + V_r \frac{\partial V_z}{\partial r} + \frac{V_\theta}{r} \frac{\partial V_z}{\partial \theta} + V_z \frac{\partial V_z}{\partial z} \right) = \mu \left(\frac{1}{r} \frac{\partial}{\partial r} \left(r \frac{\partial V_z}{\partial r} \right) \right.$$

$$\left. + \frac{1}{r^2} \frac{\partial^2 V_z}{\partial \theta^2} + \frac{\partial^2 V_z}{\partial z^2} \right) - \frac{\partial P}{\partial r} + \rho G_z \tag{6}$$

An analytic expression for the pressure distribution can be obtained from these equations when the following assumptions are made [Hughes et. al., 1989]:

1. The flow is at steady state.

2. The seal faces are axisymmetric. This allows gradients in the circumferential direction to be neglected.

3. The seal faces have no velocity component in the axial direction.

4. Velocity gradients in the radial direction can be ignored relative to velocity gradients in the axial direction.

5. Centrifugal effects can be neglected. This assumption is seen to be valid by comparing the order of magnitudes of the centrifugal force term to the pressure term from the Navier Stokes Equations. The centrifugal force term is estimated as,

$$\rho \frac{V_\theta^2}{r} = 2.25 \frac{kg}{m^3} \frac{[147 m/s]^2}{.02 \ m} = 2.4 x 10^6 N/m^3$$

The circumferential velocity is based on a rotational speed of 7,330 rad/sec for the shaft of the turbopump and a radius of 2 cm for the seal. The density of 2.25 kg/m^3 was computed from the ideal gas law for helium at a pressure of 1.38 x 10^6 N/m^2 and a temperature of 294 K. The pressure term is estimated as,

$$\frac{\partial P}{\partial r} \sim \frac{1.27x10^6 N/m^2}{.01m} = 1.27x10^8 N/m^3$$

where the pressure is assumed to decrease from 1.38 x 10^6 N/m^2 to 1.1 x 10^5 N/m^2 over a distance of 1 cm which is the approximate radial width of the proposed seal. The centrifugal term is approximately 50 times smaller than the pressure term and is therefore neglected.

6. Body forces are negligible compared to viscous forces and pressure forces.

7. The flow is laminar. This can be justified by computing the Reynold's Number which is given by the following equation;

$$Re = \rho * v_\theta * h / \mu$$

Based on a shaft speed of 7,330 rad/sec, a radius of 2 cm, a film thickness of 5 um, a density of 2.25 kg/m^3, and a viscosity of 1.99x10-5 Ns/m^2, the Reynold's number is 83. The density and viscosity are based on helium at a pressure of 1.38 x 10^6 N/m^2 and a temperature of 294 K. The Reynold's Number for which transition occurs for a similar type flow was found to be 1900 [Zuk, 1973]. Laminar flow is therefore a valid assumption.

8. The flow is isothermal. This assumption greatly simplifies calculations and is justifiable because the gas film is very thin and in contact with large masses of material with good thermal conductivity.

9. The gas film behaves as an ideal gas.

Based on these assumptions, the simplified Navier-Stokes Equations are,

$$\mu \frac{\partial^2 V_r}{\partial z^2} = \frac{\partial P}{\partial r} \qquad (10)$$

$$\frac{\partial^2 V_\theta}{\partial z^2} = 0 \qquad (11)$$

with the boundary conditions,

$$V_r = 0 \ at \ z=0 \ and \ z=h \qquad (12)$$

$$V_\theta(0) = 0 \qquad (13)$$

$$V_\theta(h) = V_{rotor} = \omega * r \qquad (14)$$

When these equations are solved the following velocity distributions result,

$$V_r = (\frac{1}{2\mu}) \frac{dP}{dr} (z^2 - hz) \qquad (15)$$

$$V_\theta = \frac{\omega r z}{h} \qquad (16)$$

The mass flow rate, or leakage of the seal, may be obtained by integrating over the film thickness in the axial direction;

$$\dot{m} = \rho \int_0^h 2\pi r v_r dz \qquad (17)$$

Substituting Equation 15 into Equation 17, and integrating results in the following equation,

$$\frac{dP}{dr} = \frac{-6\dot{m}\mu}{\pi\rho rh^3} \qquad (18)$$

Assuming a linear profile for h,

$$h = h_i + \beta(r - r_i) \qquad (19)$$

and ideal gas behavior results in the differential equation,

$$PdP = \frac{-6\dot{m}\mu RT dr}{\pi r(h_i + \beta(r - r_i))} \qquad (20)$$

Integrating the left hand side of Equation 20 from the inside to the outside pressure, and integrating the right hand side from the inside to the outside radius leads to the following equation for the mass flow rate,

$$\dot{m} = [-\pi(P_o^2 - P_i^2)(h_o - \beta r_o)^3]/12\mu RT[\ln(\frac{r_o}{r_i}) - \ln(\frac{h_o}{h_i})$$
$$+ (h_o - \beta r_o)(\frac{1}{h_o} - \frac{1}{h_i}) + \frac{(h_o - \beta r_o)^2}{2}(\frac{1}{h_o^2} - \frac{1}{h_i^2})] \qquad (21)$$

The pressure at any location within the gas film can now be found by substituting Equation 21 into Equation 20 and integrating the left hand side of Equation 21 from the

27

pressure at the inside to the pressure at the desired radial
location, and integrating the right hand side from the inside
radius to the radius of the desired location;

$$\int_{P_i}^{P(r)} P \, dP = \int_{r_i}^{r} \frac{-6 \dot{m} \mu RT \, dr}{\pi r (h_i + \beta (r - r_i))} \tag{22}$$

When the integrations are performed, the following equation
for the pressure results,

$$
\begin{aligned}
P^2 = P_i^2 + &\left[(P_o^2 - P_i^2) \left[\ln\left(\frac{r}{r_i}\right) - \ln\left(\frac{h}{h_i}\right) + (h_o - \beta r_o) \left(\frac{1}{h} - \frac{1}{h_i}\right) \right. \right. \\
&+ \frac{(h_o - \beta r_o)^2}{2} \left(\frac{1}{h^2} - \frac{1}{h_i^2}\right) \left. \right] \, / \left[\ln\left(\frac{r_o}{r_i}\right) - \ln\left(\frac{h_o}{h_i}\right) + (h_o - \beta r_o) \left(\frac{1}{h_o} - \frac{1}{h_i}\right) \right. \\
&+ \frac{(h_o - \beta r_o)^2}{2} \left(\frac{1}{h_o^2} - \frac{1}{h_i^2}\right) \left. \right]
\end{aligned}
\tag{23}
$$

This equation can be nondimensionalized in the following form,

$$
\begin{aligned}
P^* = &\left[\ln r^* - \ln(1 + \delta^* \alpha^* (r^* - 1)) + (1 - \delta^* \alpha^*) \left(\frac{1}{1 + \delta^* \alpha^* (r^* - 1)} - 1\right) \right. \\
&+ \frac{(1 - \delta^* \alpha^*)^2}{2} \left(\frac{1}{[1 + \delta^* \alpha^* (r^* - 1)]^2} - 1\right) \left. \right] / \left[\ln r_o^* - \ln(1 + \delta^* \alpha^* (r_o^* - 1)) \right. \\
&+ (1 - \delta^* \alpha^*) \left(\frac{1}{1 + \delta^* \alpha^* (r_o^* - 1)} - 1\right) + \frac{(1 - \delta^* \alpha^*)^2}{2} \left(\frac{1}{[1 + \delta^* \alpha^* (r_o^* - 1)]^2} - 1\right) \left. \right]
\end{aligned}
\tag{24}
$$

where

$$r^* = \frac{r}{r_i} \tag{25}$$

$$P^* = \frac{P^2 - P_i^2}{P_o^2 - P_i^2} \tag{26}$$

$$\alpha^* = \frac{r_i}{r_o - r_i} \tag{27}$$

$$\delta^* = \frac{\delta}{h_i} \tag{28}$$

$$\delta = h_o - h_i \tag{29}$$

The leakage rate of the seal can now be computed from Equation 21, and the pressure distribution within the gas film can be computed from Equation 23 or 24.

Figure 8 presents a graph of dimensionless pressure distributions computed from Equation 24 for various values of the nondimensional coning δ^* and for α^* equal to 1.99. This figure and Equation 24 show that the pressure distribution is uniquely determined by δ^* for given pressures P_o and P_i, and radial dimensions. The opening force, which is computed by

integrating the pressure distribution over the seal face, is also uniquely determined by specifying δ^*.

The floating component of the seal will operate at the point where the closing force is balanced by the opening force. Therefore, specifying the closing force also specifies the opening force, which in turn uniquely determines δ^*. Once δ^* is determined, the film thickness at the inside radius of the seal can be computed for a specified value of δ from Equation 29. The film thickness at any radial location is then known because the coning is specified and h is assumed to be linear. The finite element method is used to compute δ.

Seal Stiffness

The seal stiffness is an important parameter in determining the stability of the seal. The stiffness of the seal must be positive for the seal to be stable. This quantity is defined by,

$$k = -\frac{dF_{open}}{dh_i} \qquad (30)$$

When δ is constant, this equation can be formulated in terms of δ^* with the following substitutions,

$$\frac{dF_{open}}{dh_i} = \frac{dF_{open}}{d\delta^*}\frac{d\delta^*}{dh_i} \qquad (31)$$

where

$$\frac{d\delta^*}{dh_i} = \frac{d(\frac{\delta}{h_i})}{dh_i} = -\frac{\delta}{h_i^2} = -\frac{(\delta^*)^2}{\delta} \qquad (32)$$

Substituting Equation 31 and Equation 32 into Equation 30 results in the following equation for the seal stiffness,

$$k = \frac{dF_{open}}{d\delta^*}\frac{\delta^{*2}}{\delta} \qquad (33)$$

To compute the seal stiffness, F_{open} is first computed for values of δ^* between 0 and 1 at increments of 0.01 by integrating the pressure distribution over the face of the seal with Simpson's Rule. $dF_{open}/d\delta^*$ is then computed with the central difference method. Once $dF_{open}/d\delta^*$ is known, the seal stiffness can be determined from Equation 33 as a function of δ^* and δ. Because the closing force uniquely determines δ^*, the seal stiffness can also be determined as a function of the closing force and δ.

Seal Controllability

An additional concern for a controllable seal is that the thickness of the gas film should be responsive to changes in voltage applied to the seal. The controllability of the seal can be determined by examining the change in film thickness versus the change in voltage applied to the seal;

$$\frac{dh_i}{dv} = \frac{dh_i}{d\delta} \frac{d\delta}{dv} \qquad (34)$$

The film thickness can be determined from Equation 28 as a function of δ and δ^*. Once the closing force is specified, δ^* can be assumed constant which leads to the following equation for $dh_i/d\delta$,

$$\frac{dh_i}{d\delta} = \frac{d(\frac{\delta}{\delta^*})}{d\delta} = \frac{1}{\delta^*} \qquad (35)$$

Substituting Equation 35 into 34 leads to the following equation for the controllability of the seal,

$$\frac{dh_i}{dv} = \frac{1}{\delta^*} \frac{d\delta}{dv} \qquad (36)$$

The controllability of the seal consists of two parts: $d\delta/dv$ which is a function of the piezoelectric material and the configuration of the deformable face assembly, and $1/\delta^*$ which is uniquely determined by the closing force. Therefore, to maximize the controllability of the seal, the change in coning versus the change in voltage must be maximized and δ^* must be minimized.

Viscous Heat Generation

For computation of the thermal deformations of the seal, it is necessary to determine the viscous heat generation rate which occurs within the gas film. The heat generation rate per unit volume within the gas film is given by,

$$\dot{q} = \tau_{r\theta} V_\theta = \mu \frac{dV_\theta}{dz} V_\theta \qquad (37)$$

Since the radial velocity of the gas is much smaller than the angular velocity, it is neglected. Substituting Equation 16 into Equation 37, and solving for the viscous heat generation rate per unit volume at the rotating face (z=h), leads to the following equation,

$$\dot{q} = \frac{\mu \omega^2 r^2}{h} \qquad (38)$$

33

Based on a linear profile for h (see Equation 19), the rate at which heat is generated over an area of the seal face from r_a to r_b can be determined by integrating Equation 38 to obtain,

$$\dot{Q} = 2\pi\mu\omega^2 \int_{r_a}^{r_b} \frac{r^3}{h_a + \beta(r - r_a)} dr \qquad (39)$$

which results in,

$$\dot{Q} = \frac{2*\pi*\mu*\omega^2}{\beta} \left[\frac{r_b^3 - r_a^3}{3} - \frac{(\frac{h_a}{\beta} - r_a)}{2}(r_b^2 - r_a^2) + (\frac{h_a}{\beta} - r_a)^2 (r_b - r_a) \right. \qquad (40)$$
$$\left. - (\frac{h_a}{\beta} - r_a)^3 [\ln(\frac{h_a}{\beta} + r_b - r_a) - \ln(\frac{h_a}{\beta})] \right]$$

Finite Element Model

As previously discussed, the amount of coning (δ) has a direct effect on the film thickness. Therefore, it is necessary to compute δ by determining the deformations of the seal faces due to pressures, thermal strains, and voltages applied to the piezoelectric material.

The structural components of the actively controlled face seal include a piezoelectric element with a carbon face, a holder in which the piezoelectric element operates, and a rotating face. Each of these components affects the deformations of the seal faces and therefore influences δ.

34

These deformations were computed with ANSYS, a commercially available finite element program.

The finite element method is a numerical procedure used to solve differential or partial differential equations over a solution domain. This method is based on discretizing the solution domain into elements and approximating the differential equations over each element utilizing variational principles or weighted residual methods. A detailed description of the finite element method can be found in many texts [Bath, 1982; Cook, 1981].

Structural Model

Figures 9 and 10 present the finite element models of the floating component and rotating face of the seal. The model of the floating component consists of a piezoelectric element with a carbon face and a holder. The O-rings, O-ring grooves, holes for the thermocouple leads, and the epoxy which bonds the carbon face to the piezoelectric element are not included in the finite element model of the floating component (see page 65 for a discussion of the epoxy). Both models are axisymmetric with a dimension of 3.5 degrees in the circumferential direction. This angular dimension maintains reasonable aspect ratios.

The piezoelectric element is modelled by the STIF5 element of the ANSYS library [DeSalvo and Gorman, 1989]. This is a 3-

dimensional, 8-noded brick element with translational (x,y,z), voltage, temperature, and magnetic degrees of freedom at each node for a total of 6 degrees of freedom per node. The formulation of the STIF5 element is based on a variational principle [Alik and Hughes, 1970]. The carbon face, holder, and rotor are modelled with the STIF45 element of the ANSYS Library [Desalvo and Gorman, 1989]. This element is a 3-dimensional, 8-noded brick element. Each node has x, y, and z translational degrees of freedom for a total of 3 degrees of freedom per node. Two different piezoelectric materials were examined in these analyses: EDO EC-98, and PZT-5H. EDO EC-98 was found to provide slightly larger coning deformations than PZT-5H, however PZT-5H is more widely available (see Chapter V - Seal Design). The holder material was chosen to be annealed 17-4 PH stainless steel due to its corrosion resistance. The face materials were chosen to be carbon for the stationary element and tungsten carbide for the rotating face. Material properties for these elements are presented in Appendix B.

Both models are axisymmetric. The boundary conditions which enforce axisymmetry include suppressing all circumferential degrees of freedom and constraining all nodes with identical r and z coordinates to have identical displacements.

Additional boundary conditions for the floating component are imposed at the boundary between the deformable face assembly and the holder, and at the boundary between the holder and the turbopump housing. Various methods of attachment between the deformable face assembly and the holder were considered for the floating component configuration. The largest range of film thickness for a given range of voltage was obtained when the piezoelectric element was not bonded to the holder (See Chapter VI - Results). The boundary conditions which model this type of attachment are provided with the STIF52 element of the ANSYS Library. This is a gap element which behaves as a spring with infinite stiffness as it is compressed, but provides no stiffness in tension. Another method of attachment examined, was bonding the piezoelectric element to the holder. The boundary conditions which model this configuration are obtained by coupling the displacement degrees of freedom of the deformable face assembly with the displacement degrees of freedom of the holder along the boundary where the two components are attached.

The boundary condition between the turbopump and the holder is modelled by suppressing the axial motion of the holder at the point where the O-ring contacts the holder. This constraint does not exert a stress on the finite element

37

model because the pressure and spring forces which act on the floating component are balanced in the axial direction.

The boundary conditions imposed on the rotor include the two following constraints: all degrees of freedom at the inside radius of the rotor are suppressed, and the axial degrees of freedom located in the r-θ plane at the midline of the rotor are suppressed. The first boundary condition is based on the assumption that the rotor is rigidly attached to the shaft of the turbopump and the shaft is assumed to have no deformation. The second boundary condition is equivalent to assuming that the pressure and thermal load are identical on both sides of the rotor. This will generally not be true, however the error in this assumption is much smaller than those due to other assumptions made in the model (e.g. the thermal boundary conditions).

Heat Transfer Model

Thermal strains can have a significant effect on the deformations of a seal and thereby influence the coning. Therefore, a model which computes the temperatures within the structural components is necessary to predict the performance of a seal. The finite element method was used to model this temperature distribution. A description of the finite element method applied to heat transfer problems is presented in several references [Bath, 1982; Cook, 1981].

The finite element meshes used in the heat transfer analysis are identical to those used for the structural analysis which are presented in Figures 9 and 10. The STIF70 element of the ANSYS Library is used [DeSalvo and Gorman, 1989]. This element is a 3-dimensional, 8-noded brick element with temperature as the only degree of freedom per node. The finite element models used in the heat transfer analysis are axisymmetric. This condition is enforced by eliminating temperature gradients in the angular direction. The rotor is also symmetric with respect to its midline located in the $r-\theta$ plane. This symmetry condition is enforced by constraining this plane to be adiabatic (see Figure 11).

Conduction within the seal components, convection at the inside and outside radii of the components, and heat generation in the gas film are included in the model. Precise prediction of the required boundary conditions would require a detailed description of the flow field within the sealed cavity and computation of the temperatures of all the components in contact with the seal. This would require a model much larger than the one used for this project, and an extremely large computational effort. The results from this larger model would be strongly dependent on the boundary conditions assumed. However, these boundary conditions are uncertain due to the variable operating conditions of the turbopump, and the accuracy gained by the larger model would

be questionable. Therefore, considerable simplifications were made in the heat transfer analysis, as described below.

Figure 11 presents the thermal boundary conditions assumed for the heat transfer analysis. The convective boundaries include the outside and inside radii of the floating component, and the outside radius of the rotor. The conduction boundary conditions include the inside radius of the rotor where it contacts the shaft, and the location where the O-ring, which is located between the holder and the turbopump housing, contacts the holder. There is also a heat flux into the seal faces due to the viscous generation within the gas film.

The convective coefficients at the inside radius of the floating component, and the outside radius of the rotor are based on a study of a similar geometry [Gazley, 1958]. Based on this study and a preliminary seal design shown if Figure 12, a convective coefficient of 1220 $W/(m^2 K)$ is assumed at the inside radius of the floating component, and a convective coefficient 537 $W/(m^2 K)$ is assumed at the outside radius of the rotor (see Appendix C). Where the helium mixes with either the LOX or the hot turbine gases, the temperature is assumed to be the average temperature of the two fluids. This results in a fluid temperature of 382 K for the hot side of the seal and 208 K for the LOX side of the seal. The convective boundary at the outside radius of the holder is

considered at two extremes: fully insulated (H=0), and at the temperature of the helium (H=∞).

Conduction boundary conditions occur at the inside radius of the rotor where it contacts the shaft, and at the contact point between the holder and the housing. The rotor is assumed to be in close thermal contact with the shaft and is therefore fixed at the shaft temperature, assumed to be 294 K. The contact point between the O-ring and the holder is assumed to be adiabatic. This contact point is relatively far from the seal face so its effects on seal face temperatures are ignored.

For each element of the seal faces adjacent to the gas film, there is a heat flux into the element due to the viscous generation within the film. The model used to compute these heat transfer effects is based on several simplifying assumptions. First, all viscous heat generation within the gas film from is due to the angular velocity of the rotor. Equation 40 can then be used to compute the heat generation rate. Second, all heat generated within the gas film flows into the seal faces. This is generally valid for face seals because the gas film is very thin and in contact with the seal faces which have relatively high thermal conductivities. Third, the heat is apportioned between the seal faces in direct proportion to their relative thermal conductivities. In reality, the proportion of heat which flows into each seal

face is affected by its geometry, thermal conductivity, and thermal boundary conditions. However, the model was considerably simplified by apportioning the heat based on the relative thermal conductivities of the seal faces and the errors resulting from this assumption are less significant than the errors introduced by other approximations made in the model. The heat flow per node for the elements of the seal faces is then computed by dividing the heat flow for each element equally between the nodes.

Computation of Seal Performance

With the finite element model which computes the coning, and the fluid mechanics model which computes the pressure distribution within the gas film, it is now possible to compute the film thickness and leakage rate of the seal. Figure 13 presents the iterative procedure which was used to determine the performance of the seal.

The first step is to compute the temperature distribution within the seal components which results from the thermal boundary conditions. This is done with the finite element program ANSYS. No viscous heat generation is included for this step.

The second step is to determine δ^* which is found by first computing the closing force from Equation 1. As described above (see page 29), the closing force uniquely determines δ^*.

The computational procedure is to assume a value for δ^*, compute the pressure profile and opening force which result from the assumed δ^*, compare the opening force to the closing force, and use the modified regula falsi method (presented in Appendix D) to modify the value of δ^*. This procedure is then repeated until the difference between the closing force and opening force is less than 0.001 N. The temperature distribution which was computed from the previous step is also read, and these temperatures are written to an ANSYS batch file to compute the deformation of the seal components.

For the third step, the deformations of the seal faces are computed with ANSYS. These deformations are due to voltage, thermal, and pressure loads. At this stage, the thermal load does not include viscous heat generation.

Once the deformations of the seal faces are known, the film thickness can be computed in the fourth step. The faces are assumed to have a linear profile and δ is computed from Equation 29. From the coning, the film thickness at the inside radius of the seal faces can be determined from Equation 28, which then determines the viscous heat generation rate produced within the film. The viscous heat generation rate is written to an ANSYS batch file for use in the thermal analysis of the next step.

The fifth step consists of computing the temperature profiles within the seal components with ANSYS. Viscous heat

generation as well as the thermal boundary conditions are now accounted for.

For the sixth step, the temperature profiles computed in the previous step are read from a data file, and an ANSYS batch file is written to compute the deformations of the seal faces.

New deformations of the seal faces are now computed in the seventh step with ANSYS. These deformations also include voltage and pressure loads.

The eighth step consists of computing a new film thickness based on the coning which is produced by the deformations determined from the previous step, and computing a new viscous heat generation rate based on the modified film thickness. This new film thickness is compared with the old film thickness, and the new temperature distribution is compared with the old temperature distribution. If the film thicknesses differ by less than .001 um, and the temperature distributions differ by less then 1 K, then the solution for this voltage level is assumed to have converged. If this convergence criterion is not met, the computational procedure resumes at step 5. For low voltage levels which result in very thin gas films, it is necessary to relax the coning deformation to achieve convergence,

$$\delta = \delta_{old}(1-\kappa) + \delta_{new}\kappa \qquad\qquad (41)$$

where κ is chosen to be between 0 and 1 (typically 0.6). Because the coning is relaxed, large changes in film thickness are prevented, which in turn prevents large increases in the viscous heat generation rate. This helps the solution to converge when the viscous dissipation becomes large as a result of small film thicknesses. If the film thickness becomes too thin (less than .001 um) the faces are assumed to have contacted and the computational procedure is stopped.

In the ninth step, a new voltage load is written to an ANSYS batch file and the computational procedure resumes at the fifth step. If the results from all the voltage levels have been computed, then the computations are finished. Five voltage loads were applied for each computational run: 5000, 3000, 1000, 500, and 100 volts. Best performance for this computational procedure was achieved when the voltage loads were applied in decreasing magnitude. As each solution was obtained, it was used as an initial guess for the computation of the next voltage load.

The results obtained from the mathematical model include the film thickness at the inside radius of the seal faces, the coning, the leakage, the temperature profiles of each seal

component, and the pressure profile within the gas film. These results were obtained for each specified voltage level.

CHAPTER V

SEAL DESIGN

The design process for this seal involved formulating a preliminary configuration which met the size constraints previously described, evaluating the performance with the mathematical model (described in Chapter IV - Mathematical Model), and revising the design to improve the performance of the seal. The major objectives for seal performance were: to maximize the range of film thickness for the range of applied voltage, to produce film thicknesses on the order of a few microns (1-4 um) as the voltage approached 0, and to ensure stable operation of the seal. The detailed designs which follow are a final version achieved through this iterative process.

Design of the Seal Rotor

The detailed design of the rotor is presented in Figure A-1. The primary considerations for this design were to ensure that the rotor can withstand the stresses which are imposed on it, and to prevent contact between the LOX and hot gases. The material for the rotor was selected to be tungsten carbide which is extremely strong. Tungsten carbide also has

very good wear characteristics when mated with a carbon-graphite face.

The primary strength consideration for the rotor was to ensure that it can withstand the centrifugal stresses which are produced by a rotational speed of 7330 rad/sec. To compute these stresses, a finite element analysis was performed of the rotor presented in Figure 12, and the principal stresses were computed. The maximum principal stress, which occurred at the inside radius of the rotor, was 70.8 MPa. A strength theory generally used for brittle materials (such as tungsten carbide) is to compare the ultimate tensile strength of the material with the maximum principal stress [Budynas, 1977]. For tungsten carbide, the bending strength (which is an indirect measure of the tensile strength) is 1700 Mpa [Cleaver, 1988] which is much larger than the principal stress previously computed. Therefore, a tungsten carbide rotor is strong enough to withstand the centrifugal stresses produced by a shaft speed of 7330 rad/sec.

Leakage between the seal rotor and the turbopump shaft will be prevented by the interference fit and the secondary seal located at the inner radius of the rotor.

Design of the Floating Component

The floating component consists of the holder, spring, deformable face assembly, and secondary seals.

Design of Holder

The design of the holder is presented in Figure A-2. The major consideration for the holder was to define the geometry such that the required balance ratio was produced. The balance ratio, defined in Equation 3 and shown in Figure 2, directly affects the closing force which acts on the floating component of the seal (see Chapter V - Mathematical Model). The closing force has three primary effects on the operation of the seal: it determines the stability, controllability (the change in the film thickness versus the change in the voltage applied to the piezoelectric element), and film thickness. Stability considerations indicate that the closing force should be maximized while controllability considerations indicate that the closing force be minimized. Based on results from the mathematical model (see Chapter VI - Results), a balance ratio of 0.65 was chosen which, with the selected spring force, produces a closing force of 560 N. This represents a reasonable tradeoff between stability and responsiveness of the seal.

The material for the holder was selected to be 17-4 ph steel which is corrosion resistant and has a relatively high

modulus of elasticity. This will minimize deformations of the holder due to the pressure load. Such deformations could adversely affect the performance of the seal.

A slot for a secondary seal is machined into the holder. This secondary seal will prevent helium leakage through the gap formed by the outside radius of the deformable face assembly and the holder.

Selection of the Spring

The spring, in conjunction with the pressure load, supplies the closing force which acts on the floating component of the seal. As described above, the closing force has a direct effect on the performance of the seal. The spring must be small enough to fit in the gap formed by the backside of the holder and the wall of the seal cavity. An additional consideration was that the spring must be of reasonable cost and commercially available, to facilitate ease of construction of the experimental seal.

Based on these considerations, a wave spring washer was chosen for this application. This type of spring is relatively soft and can provide the necessary force of 62 N (see Chapter VI - Results). Wave spring washers can fit in relatively small gaps and are widely commercially available. Other types of springs (e.g. Belville washers) are much

stiffer and provide closing forces which are too large for this application.

Design of Deformable Face Assembly

The deformable face assembly consists of a piezoelectric element and carbon face which is bonded to the piezoelectric element with epoxy. The coning of the carbon face is controlled by applying an electric field to the piezoelectric element. This deforms the piezoelectric element which, in turn, deforms the attached carbon face. As previously described, the coning has a direct effect on the film thickness of the seal. Therefore, the range of film thickness experienced by this seal will be related to the range of coning provided by the deformable face assembly. The major design objective for the deformable face assembly was therefore, to maximize the range of coning for the range of voltage applied to the piezoelectric element.

The type of deformation produced in a piezoelectric material depends on the polarity of the applied voltage relative to the direction of the poling axis. The piezoelectric effect is produced in various materials (e.g. lead zirconate titanate) by a polarizing treatment (during the manufacturing process) in which a d.c. electric field is applied to the material. The direction of the d.c. field defines the poling axis for the material. When electric

51

fields of the same direction as the poling axis are applied to the material, the material expands in this direction. Conversely, the material contracts if electric fields are applied in a direction opposite to the poling axis. Shear deformations can also be produced by applying electric fields perpendicular to the poling axis.

Coning deformation, which is defined in Equation 29 and shown in Figure 1, can be obtained from various configurations of piezoelectric elements. The amount of coning deformation of the carbon face depends most directly on the configuration of the deformable face assembly, the type of piezoelectric material, the sizes of the piezoelectric element and carbon face, and the magnitude of the applied electric field.

Three configurations of piezoelectric elements were examined for use in this seal: the shear mode, the bimorph, and the axial mode. The coning deformations produced by these configurations were computed with the finite element method (described in Chapter IV - Mathematical Model).

Figure 14 presents a configuration in which a coning deformation of the carbon face is produced by a shear deformation of the piezoelectric element. This figure represents a cross sectional view of the deformable face assembly (see Section A-A of Figure 15). The shear deformation is produced by applying an electric field in the r-direction which is perpendicular to the poling axis. The

electric field is produced by bonding electrodes to the outside and inside radius of the piezoelectric element, and then applying a voltage to these electrodes (see Figure 14).

Figure 16 presents a configuration in which coning deformation is produced with a bimorph. A bimorph consists of two piezoelectric elements: one of the elements is poled in the positive r-direction while the other is poled in the negative r-direction. The two piezoelectric elements are bonded together, and a carbon face is bonded to one of the faces of the bimorph. Electrodes are bonded to the outside and inside radii of the piezoelectric elements and a voltage is applied to these electrodes. This creates an electric field in the radial direction which causes one of the piezoelectric elements to expand in the radial direction while the other contracts. This deformation causes a coning deformation of the carbon face, as shown in Figure 16.

An axial mode of deformation which produces a coning deformation is presented in Figure 17. For this mode, the poling axis is in the z-direction and the applied electric field is in the same direction. The electric field is produced by bonding electrodes to the faces of the piezoelectric element perpendicular to the z-direction, and by applying a voltage to these electrodes. When the element is clamped at the outside radius, the piezoelectric element will deform at the inner radius in the z-direction while no

deformation will occur at the outer radius. This deformation will produce coning in the carbon face which is bonded to the piezoelectric element.

Based on results from the finite element model (see Chapter V - Results), the shear mode produced the largest coning for the dimensions appropriate to this seal design. Therefore, the shear mode was chosen for use in the final seal design.

The type of piezoelectric material directly affects the magnitude of the coning deformation produced by a given voltage. There are a large number of commercially available piezoelectric materials which are tailored to suit various applications. The governing criterion for this design was to obtain the maximum amount of deformation for a given voltage. The strains induced as a function of the electric field can be determined by examining the [d] matrix of the piezoelectric material (see Appendix B). The coefficients of the [d] matrix which govern the shear and axial mode of deformation are the d_{15} and d_{33} coefficients, respectively; the magnitude of deformation is proportional to the magnitude of these coefficients. The piezoelectric material EC-98 produced by the EDO Corporation was found to have the largest d_{15} and d_{33} coefficients.

An additional criterion for the piezoelectric material, which affects the coning deformation, is the ability of the

material to support large electric fields. The magnitude of the coning deformation increases as the voltage is increased. However, if excessive voltages are applied, the material breaks down and loses its piezoelectric effect. The material which supports the largest electric field is also EDO EC-98.

Based on these criteria, EDO EC-98 is the material best suited for use in the deformable face assembly. A second material, PZT-5H produced by the Vernitron Corporation, was also examined. An advantage of the latter material is that several companies produce a comparable material and it is therefore widely available. This material may be used for a backup choice during the experimental testing due to its lower cost.

The detailed design of the deformable face assembly is presented in Figure A-3. As previously discussed, the shear mode was chosen for use in this assembly. Finite element analyses (see Chapter VI - Results) indicated that increasing the axial thickness of the piezoelectric element with respect to the carbon face increased the coning deformation. For the shear mode of deformation, the coning deformation is also increased as the radial thickness of the element is increased. The dimensions presented in Figure A-3 represent a trade off between maximizing the dimensions to enhance the range of coning deformation while limiting the dimensions to meet the size constraints.

The deformable face assembly floats in the holder and is restrained only through compression of the O-ring which is located between the deformable face assembly and the holder. Results from the mathematical model indicated that the largest range of coning deformation was obtained for the shear mode when the piezoelectric element was unrestrained. The compression fit utilized for this design minimizes the constraints which act upon the deformable face assembly and maximizes the coning deformation.

Figure A-3 also shows the electrodes for the deformable face assembly. These are located at the outside and inside radii of the piezoelectric element. The poling axis for the piezoelectric element is parallel to the shaft of the turbopump. When voltage is applied to the electrodes, an electric field perpendicular to the poling axis results, which produces the shear deformation. The piezoelectric element is encased in an epoxy coating to prevent breakdown of the electric field. Such breakdown would occur if the electrodes contacted other seal components.

An additional consideration for the deformable face assembly is that an initial coning may be required in the seal faces to prevent contact at low voltage levels. Based on results from the mathematical model, the seal faces contact at low voltage levels for some of the thermal boundary conditions which were assumed (see Figure 20 and 21 of Chapter VI –

Results). Such contact can be prevented by machining an initial positive coning into the seal faces (see Figure 22 of Chapter VI - Results).

Secondary Seals

There are two secondary seals required for each floating component of the face seal: an O-ring located between the deformable face assembly and the holder, and an O-ring located between the holder and turbopump housing. The deformable face assembly is not attached to the holder so a secondary seal between the holder and deformable face assembly is necessary to prevent helium leakage between these two elements. The secondary seal between the holder and turbopump housing prevents helium leakage through the gap formed by these elements. The O-rings are made from Buna N, which is adequate for operation of a laboratory test rig at room temperature (294 K).

CHAPTER VI

RESULTS

Determination of Closing Force

As described above (see Chapter III - Mathematical Model), the seal stiffness and controllability are strongly dependent on δ^*, which is uniquely determined by the closing force. The seal stiffness affects the stability of the seal and also provides an indication of how the operation of the seal changes as the closing force is perturbed from its design value. Therefore, a first step in the design of the actively controlled seal is to determine the closing force which optimizes the stiffness and controllability of the seal.

A positive seal stiffness is a necessary condition for stable seal operation. The relation between seal stiffness and stability can be understood by examining Equation 30, and by considering a slight decrease in the film thickness between the seal faces. For a seal with positive stiffness, this decrease in film thickness produces a larger opening force. The forces acting on the seal are now unbalanced and the increased opening force will push the faces of the seal apart to restore the previous film thickness. Therefore, the seal will be stable. Conversely, for a negative stiffness, a

decrease in the film thickness produces a decrease in the opening force. The decreased opening force will result in a further decrease in film thickness and the seal will be unstable.

The sign of the seal stiffness is uniquely determined by the sign of δ^*, as can be seen from Equation 33. Figure 8 shows that as δ^* increases, the average pressure within the gas film increases, and therefore the opening force increases. Hence, $dF_{open}/d\delta^*$ is always positive. The sign of the seal stiffness is therefore determined by the sign of δ; a positive δ results in a positive seal stiffness. Equation 28 shows that δ and δ^* must have the same sign because a negative film thickness is physically unrealistic. Therefore, δ^* must be positive for the seal stiffness to be positive.

In addition to influencing stability, seal stiffness also determines how deviations in the closing force from the design value affect the performance of the seal. Such deviations could be due to manufacturing tolerances of the wave spring washers, fabrication and installation tolerances of the seal, the additional spring force due to the O-rings, and others as well. If these changes in the closing force produce large changes in the film thickness of the seal, it would be very difficult to produce a seal with predictable and repeatable operation. The effect of such perturbations on the film

thickness can be understood by examining the inverse of the seal stiffness;

$$\frac{1}{k} = \frac{-dh_i}{dF_{open}}$$ (42)

As the inverse of the seal stiffness decreases, the change in film thickness due to perturbations in the closing force decreases. Figure 18 presents a graph of the inverse of the seal stiffness for two different values of coning: 1 um and 3 um. This figure shows that for values of the closing force below 550 N, 1/k is large, which indicates that large changes in film thickness occur due to small changes in the closing force.

The closing force also strongly affects the controllability of the seal. Equation 36 shows that the controllability of the seal is proportional to $1/\delta^*$. Figure 18 shows that the controllability of the seal decreases as the closing force increases.

It is therefore seen that the stiffness and controllability of the seal impose conflicting requirements on the selection of the closing force. Stiffness considerations indicate that δ^* should be maximized while controllability considerations require that δ^* should be minimized. Based on Figure 18, an initial closing force of 560 N was chosen as a

60

compromise. For this closing force, δ^* is equal to 0.25 and 1/k is less than 0.5 um/N for the two coning values. This value of the closing force represents a reasonable tradeoff between stability and controllability of the seal.

Design of Deformable Face Assembly

The deformable face assembly consists of a piezoelectric material with electrodes, and a carbon face which is bonded to the piezoelectric material. This assembly deforms when voltage is applied and produces the coning deformation which is required to control the film thickness. The controllability of the seal strongly depends on the magnitude of the coning deformation which can be obtained from the deformable face assembly. Thus, the major objective for the design of the deformable face assembly is to maximize the coning deformation which can be produced.

As previously described (see Chapter V - Seal Design), the piezoelectric material EC-98 produced by the EDO Corporation is best suited for use in the deformable face assembly. Initially, three deformation modes of the deformable face assembly were considered for possible use: the shear mode, the bimorph, and the axial mode (see Figures 14, 16, and 17). For each of these modes, the effects of various parameters on the coning deformation were studied. These parameters include type of material, the size of the piezoelectric element, the

thickness of the carbon face, the direction of the poling axis relative to the applied voltage, and the amount of voltage applied. The coning deformation was computed with ANSYS, a commercially available finite element program. Each configuration was evaluated based on the maximum amount of coning which could be produced by the maximum allowable voltage applied to the deformable face assembly.

Shear Mode

Figure 14 presents a sketch of the shear mode of deformation and Table 1 presents a summary of the results obtained for that mode. The dimensions of the finite element models, presented in Table 1, refer to a ring shaped configuration (see Figure 15) for which the inside radius is 0.159 cm. The finite element models are axisymmetric with a circumferential dimension of 10 degrees. The boundary conditions for the shear mode configurations are: the inside radius is fully clamped and all other edges are free.

Cases 1 and 2 present the effect of the material type on the coning deformation. EDO EC-98 produces a coning deformation of 0.8 um as compared to 0.7 um for the Vernitron PZT-5H material. A comparison of Cases 2 and 3 presents the effect of the direction of the poling axis and applied voltage on the coning deformation. This comparison is used to determine the optimum direction of the electric field. For case 2, the

poling axis is in the axial direction and the voltage is applied in the radial direction. For case 3, the poling axis is in the radial direction and the voltage is applied in the axial direction. The corresponding coning deformation are the same, both 0.7 um. Therefore, for the geometries of Cases 2 and 3 which have approximately square cross-sections, the poling axis can be either in the axial or in the radial direction, with no difference in the coning deformation.

Case 4 presents a geometry in which the width of the piezoelectric material is half as large as for Case 1. The coning deformation for this case is approximately twice as large as for Case 1. The reduced width of the piezoelectric element results in a more flexible structure which causes the coning deformation to increase.

Case 5 presents the maximum coning deformation when the maximum recommended voltage is applied to the piezoelectric element for the configuration of Case 1. The maximum recommended electric field for EDO EC-98 in a direction perpendicular to the poling axis is 900 v/mm. This electric field corresponds to a voltage of 5715 volts for the Case 1 configuration. Such a voltage produces a coning deformation of 4.7 um.

Cases 6-9 present the effects of bonding carbon faces of various thicknesses to the piezoelectric element. The carbon face causes a reduced coning deformation when compared with

similar configurations in which no carbon face is attached. A comparison between cases 6 and 7 shows that as the thickness of the carbon face increases, the coning deformation decreases. Cases 7 and 8 show that as the width of the piezoelectric element decreases, the coning deformation also decreases. The maximum coning deformation for a carbon face of 0.3 cm thick is given in case 9 and is 3.9 um. Based on these results, the coning deformation increases as the axial width of the piezoelectric element increases relative to the axial width of the carbon face.

Bimorph

Figure 16 presents a configuration in which a coning deformation is produced with a bimorph (see Chapter V - Seal Design). The dimensions of the various configurations and the results are presented in Table 2. Each configuration is similar to Figure 15 with an inside radius of 0.159 cm, and a circumferential dimension of 10 degrees. The boundary conditions for these models are: the inside radius is fully clamped and all other edges are free.

Cases 1 and 2 present the effects of the material type on the coning deformation. The EDO EC-98 material produces a coning deformation of 0.9 um as compared to 0.7 um for the PZT-5H material.

The effects of the size of the piezoelectric element can be seen in cases 2, 3, and 4. Case 3 presents a bimorph which is half as wide as that of case 2. The coning deformation for case 3 increased to 1.3 um from 0.7 um for Case 2. Case 4 presents a bimorph for which the height is reduced by a factor of 2. The coning deformation decreased to 0.4 um for this case.

Case 5 presents the maximum coning deformation when the maximum recommended voltage is applied to the piezoelectric element. The electric field limit for the EC-98 material when the field is applied in a direction opposite to the poling axis is 450 v/mm. This corresponds to a voltage of 2858 for the configuration presented in Case 5. The coning deformation produced by this voltage is 2.4 um. This deformation is approximately half as large as the maximum coning deformation obtained from the shear configuration with identical axial and radial dimensions.

Cases 6-8 present the effects of bonding a carbon face to the piezoelectric element. The carbon face reduces the coning deformation when compared to similar configurations in which no carbon face is attached. The maximum coning deformation for a carbon face 0.3 cm thick is given in case 9 and is 0.9 um. This is significantly less than the maximum coning produced by the shear mode with identical axial and radial dimensions (3.9 um).

Axial Mode

Figure 17 presents a configuration in which a coning deformation is produced with the axial mode of deformation (see Chapter V - Seal Design). The dimensions of the various configurations and the results are presented in Table 3. Each configuration is similar to Figure 15, axisymmetric, with an inside radius of 0.159 cm, and a circumferential dimension of 10 degrees. The boundary conditions for the axial mode are presented in Figure 17: the inside radius is fully clamped, the edge of the seal opposite to the seal face is constrained in the axial direction, and all other edges are free.

A comparison of Cases 1 and 2 show the effect of the width of the piezoelectric element on the coning deformation. When the width is reduced by a factor of two, the coning deformation remains constant. It does not change due to two opposing effects: the larger electric field, and the increased stiffness. When the width is reduced by a factor of two and the voltage remains constant, the electric field is doubled, which increases the deformation of the piezoelectric element. The reduced width of the material also stiffens the material, which decreases the deformation. These two effects offset one another and the coning deformation is not changed.

Case 3 presents the maximum coning deformation when the maximum recommended voltage is applied to the piezoelectric

element for the case when no carbon face is attached. The voltage limit for the axial mode for EC-98 is 5715 v. The coning deformation produced by this voltage is 3.5 um which is less than the maximum coning obtained from the shear mode for a similar configuration.

Cases 4-7 present the effects of bonding a carbon face to the piezoelectric element. The carbon face causes a reduced coning deformation. The maximum coning deformation for a carbon face of 0.3 cm thick is given in case 6 and is 2.6 um. This is less than the maximum displacement for the corresponding configuration of the shear mode but greater than that for the bimorph.

Comparison of Deformation Modes

Table 4 presents a comparison of the deformations for various configurations and loadings. The base case is case 1 for the three different deformation modes. All analyses presented in Table 4 were performed with the material EC-98. The shear mode consistently produced larger coning deformations when a carbon face was attached than either the axial mode or bimorph. Therefore, the shear mode was chosen for the deformable face assembly.

Seal Performance

The finite element models presented in Figures 10 and 11 in conjunction with the computational scheme presented in

67

Figure 13 were used to determine the performance of the seal. The goal of this design is to obtain film thicknesses on the order of a few microns (1-4 um), and to maximize the range of film thickness which can be produced by the seal. The dimensions utilized for these analyses are preliminary dimensions and are shown in Figure 12.

Initial Considerations

Initially it was necessary to determine which components should be included in the finite element model of the seal. The seal consists of a holder, piezoelectric element, carbon face, two O-rings, and a rotating face. The O-ring located between the holder and housing was assumed to constrain the axial motion of the seal. The effects of the O-ring located between the deformable face assembly and the holder were ignored.

The effects of the epoxy which bonds the carbon face to the piezoelectric material, and which insulates the back side of the piezoelectric element were also neglected. To evaluate the validity of this assumption, a thin film (0.025 cm) of epoxy was included in a model of the deformable face assembly. For this model, the coning deformation produced by a voltage of 5000 V was 3.46 um. For the model with no epoxy film, the coning deformation produced by a voltage load of 5000 V was 3.47 um. Since the difference in the coning deformation is

only 0.01 um, the epoxy was not included in the finite element model.

It was also necessary to determine the optimum boundary conditions for the deformable face assembly. The boundary conditions which were evaluated were those corresponding to a deformable face assembly which floats in the holder, and a deformable face assembly which is bonded to the holder at the outside radius. The effects of these boundary conditions can be evaluated from Figure 19 which presents plots of film thickness versus voltage. The seal with the floating assembly produced a larger range of film thicknesses than that with the clamped assembly. The floating face assembly will also enhance the ability of the seal to track the runout present in the rotating face due to manufacturing tolerances of the turbopump. The seal was therefore designed with a floating deformable face assembly.

Effects of Thermal Boundary Conditions

Once the finite element model was established, several analyses were performed for various thermal boundary conditions. Figure 20 presents the film thickness versus voltage for cases where the holder is insulated at the outside radius. There are 5 curves plotted. For three of them, the temperature of the hot gas at the inside radius of the holder was varied to model the hot side (temperature=382 K), the cold

side (temperature=208 K), and room temperature (temperature=294 K). The additional two curves neglect thermal deformations and show the performance due to voltage load only, and due to a combined pressure and voltage load. This figure indicates that the thermal boundary conditions at the inside radius of the floating component have a significant effect on the performance of the seal. The performance curves predict a decrease in film thickness for the various voltage levels as the temperature of the fluid at the inside radius of the floating component increases.

Figure 21 presents film thicknesses versus voltage for cases where the temperature at the outside radius of the floating component is fixed at 294 K (the temperature of the helium flowing into the seal cavity). This boundary condition would be approached as the convective coefficient at the outside radius of the floating component approaches infinity. The film thicknesses for the various voltage levels increase as the temperature of the fluid at the inside radius of the floating component increases. This trend is opposite to that presented in Figure 20. Thus, the thermal boundary conditions at the outside radius of the holder are seen to strongly affect the performance of the seal.

Effects of Initial Coning

An additional means of influencing the performance of the seal is to pre-machine an initial coning into the seal faces. Figure 22 presents five performance curves for cases where the floating component is insulated at the outside radius. For three of these curves, the temperature of the hot gas at the inside radius of the holder was varied to model the hot side (temperature=382 K), the cold side (temperature=208 K), and room temperature (temperature=294 K). The performance of the seal with an initial coning of 1 um for hot side and room temperature conditions is also presented in this figure. The associated leakage rates for these cases are presented in Figure 23. Figures 22 and 23 show that the initial coning increases the film thickness as compared to the cases with no initial coning. Therefore, pre-machining an initial coning into the seal faces could be used to prevent contact of the seal faces for low voltage levels. Conversely, pre-machining an initial negative coning could be used to reduce the film thicknesses if a seal leaked excessively.

Variable Pressure Operation

Figure 24 presents the performance curves of the seal for various sealed pressures. The range of film thickness which can be produced by the controllable seal decreases as the sealed pressured decreases. Physically, this degradation in

performance at lower pressures can be explained by considering the control mechanism for the seal. The control for the seal is produced by varying the opening force of the seal by means of the adjustable coning. The controllability of the seal therefore depends on the magnitude of the variation in the opening force which can be produced by the seal. The opening force for a hydrostatic seal is generated by the sealed pressure and as the sealed pressure decreases, the magnitude of the variation in the opening force which the seal can produce also decreases. This results in a degradation in the controllability of the seal at lower sealed pressures.

Comparison of Piezoelectric Materials

Figure 25 compares the performance of the two different piezoelectric materials used in this analysis (EDO EC-98 and PZT-5H) for voltage and pressure loading only. Larger shear deformations occur for the EC-98 material as compared to the PZT-5H material for a given voltage, due to its higher d_{15}. This produces a slightly larger film thickness for the EC-98 material. The major advantage of the EC-98 material however, is its ability to withstand higher electric fields (900 V/mm) compared to the PZT-5H (450 v/mm). The larger range of voltage of the EC-98 approximately doubles the range of film thickness.

Dynamic Stability Considerations

An additional consideration for mechanical seals which operate at high rotational speeds is the dynamic stability of the seal. Dynamic instabilities of the components could result in excessive leakage and failure of the seal.

A dynamic stability analysis of the designed seal is beyond the scope of the present study. However, an indication of the dynamic stability can be obtained from a NASA report which concerns shaft seals for liquid rocket engine turbopumps [Burcham, 1978]. This report is based on extensive experience with rotating shaft seals for liquid rocket engine turbopumps and is intended to provide guide lines for seal design. It suggests that the secondary seals generally provide enough damping to eliminate dynamic instabilities.

Performance of Final Design

The previous analyses are based on a seal with the dimensions shown in Figure 12. However for the final detailed seal design (presented in Appendix A), the dimensions were slightly changed so secondary seals of standard sizes could be used. To determine the effects of these changes, one additional analysis was performed. The balance ratio for the final design is 0.658 and the spring force is 70 N. These factors produce a closing force of 630 N, which result in a

value of 0.25 for δ^*, the same δ^* as found in the preliminary seal design.

Figure 26 presents the performance of the final seal design for the following cases: hot side (382 K), room temperature (294 K), room temperature with an initial coning of 1 um, cold side (T=208 K), and cold side with an initial coning of -2.5 um. For room temperature conditions, the viscous heat generation is based on a shaft rotational speed of 4,189 rad/sec (40,000 rpm), which will be the maximum speed of the experimental test rig. The performance of the final seal design is seen to be similar to the performance of the seal with the preliminary dimensions.

CHAPTER VII

CONCLUSIONS

The results presented in this study indicate that an actively controlled seal for the helium purge assembly of a LOX turbopump is feasible. Two of the major goals of the design are to establish a film thickness on the order of a few microns and to maximize the range of film thickness which can be produced by the seal. Both of these goals appear to be attainable with the seal design presented in Appendix A.

The results shown in Figure 26 indicate that film thicknesses on the order of a few microns can be obtained with the proposed seal design. Thermal deformations could adversely affect the performance of the seal, however these effects can be minimized by pre-machining an initial coning into the seal faces.

A film thickness range of approximately 10 um is predicted for the proposed seal design. The range of film thickness is shown to be strongly dependent on the closing force. If the closing force deviates significantly from the design value, the performance of the seal will be adversely affected. Therefore, successful seal operation will depend on meeting manufacturing tolerances to minimize these deviations.

The construction of the test rig has been completed and preliminary testing is now underway (see Appendix E). The coning deformations produced by the deformable face assembly are in good agreement with those predicted by the finite element model. Static pressure tests have been performed with the assembled test rig. These tests have indicated that the large tolerances produced by the electrical insulation on the deformable face assembly may cause leakage through the adjacent o-ring. A holder manufactured from a nonconductive material would eliminate the need for the electrical insulation. Various nonconductive materials are currently being considered as a construction material for the holder.

Table 1. Shear Mode						
Case	Width (cm)	Height (cm)	Voltage and Direct.	Thk. of Carbon (cm)	Mater.	Coning (um)
1	.635	.635	1000-r	0	PZT-5H	.74
2	.635	.635	1000-z	0	PZT-5H	.72
3	.318	.635	1000-z	0	PZT-5H	1.41
4	.635	.635	1000-r	0	EC-98	.83
5	.635	.635	5715-r	0	EC-98	4.72
6	.635	.635	1000-r	.15	EC-98	.78
7	.635	.635	1000-r	.30	EC-98	.68
8	.318	.635	1000-r	.30	EC-98	.55
9	.635	.635	5715-r	.30	EC-98	3.89

Table 2. Bimorph
Case	Width (cm)	Height (cm)	Voltage	Thk. of Carbon (cm)	Mater.	Coning (um)
1	.635	.635	1000	0	PZT-5H	.67
2	.635	.635	2000	0	PZT-5H	1.27
3	.635	.318	1000	0	PZT-5H	.41
4	.318	.635	1000	0	PZT-5H	1.24
5	.635	.635	1000	0	EC-98	.85
6	.635	.635	2858	0	EC-98	2.42
7	.635	.635	1000	.15	EC-98	.52
8	.635	.635	1000	.30	EC-98	.32
9	.318	.635	1000	.30	EC-98	.36
10	.635	.635	2858	.30	EC-98	.93

Table 3. Axial Mode						
Case	Width (cm)	Height (cm)	Voltage (z-dir)	Thk. of Carbon (cm)	Mater.	Coning (um)
1	.635	.635	1000	0	EC-98	.61
2	.635	.635	2000	0	EC-98	1.21
3	.318	.635	1000	0	EC-98	.60
4	.635	.635	5715	0	EC-98	3.47
5	.635	.635	1000	.15	EC-98	.51
6	.635	.635	1000	.30	EC-98	.45
7	.635	.635	5715	.30	EC-98	2.57

Table 4. Comparison of Deformation Modes						
Case	Width (cm)	Height (cm)	Volt.	Thk. of Carbon (cm)	Coning (um)	Mode
Base Case	.635	.635	1000	0	.61	Axial
					.83	Shear
					.85	Bimorph
Maximum E-Field	.635	.635	5715	0	3.47	Axial
			5715		4.72	Shear
			2858		2.42	Bimorph
Carbon Face .15 cm	.635	.635	1000	.15	.51	Axial
					.78	Shear
					.52	Bimorph
Carbon Face .30 cm	.635	.635	1000	.30	.45	Axial
					.71	Shear
					.32	Bimorph
Carbon Face .30 cm Width= w/2	.318	.635	1000	.30	.48	Axial
					.55	Shear
					.36	Bimorph
Carbon Face .30 cm Maximum E-Field	.635	.635	5715	.30	2.57	Axial
			5715		3.89	Shear
			2858		.93	Bimorph

Table 5. Piezoelectric Material Properties		
Material Property	PZT-5H	EC-98
d_{31}	-274×10^{-12}	-312×10^{-12}
d_{33}	593×10^{-12}	730×10^{-12}
d_{15}	741×10^{-12}	825×10^{-12}
s_{11}	16.5×10^{-12}	16.3×10^{-12}
s_{33}	20.7×10^{-12}	21.1×10^{-12}
s_{12}	-4.78×10^{-12}	-5.6×10^{-12}
s_{13}	-8.45×10^{-12}	-8.62×10^{-12}
s_{44}	23.7×10^{-12}	44.3×10^{-12}
s_{66}	42.5×10^{-12}	43.8×10^{-12}
ϵ_{11}^{r}	0.50×10^{-8}	4.86×10^{-8}
ϵ_{33}^{r}	1.30×10^{-8}	4.86×10^{-8}
ϵ_{11}^{i}	-3.01×10^{-10}	-9.73×10^{-10}
ϵ_{33}^{i}	-2.60×10^{-10}	-9.73×10^{-10}
$\tan \zeta$	0.02	.02

TABLE 6   Piezoelectric Properties - Ansys Format
Material Property	PZT-5H	EC-98
e_{31}	-6.62	-3.77
e_{33}	23.24	31.52
e_{15}	17.03	18.61
c_{11}	12.72×10^{10}	15.96×10^{10}
c_{33}	11.74×10^{10}	13.87×10^{10}
c_{12}	8.02×10^{10}	11.39×10^{10}
c_{13}	8.47×10^{10}	11.17×10^{10}
c_{44}	2.30×10^{10}	2.26×10^{10}
c_{66}	2.35×10^{10}	2.28×10^{10}

Table 7. Thermal Expansion Coefficients of Piezoelectric Material

Temperature (C)	α_1 (10^{-6}/C)	α_3 (10^{-6}/C)
0	1.0	4.0
50	1.4	4.0
100	2.0	3.0
150	2.7	1.0
200	3.3	-1.6
250	3.9	-4.2

Table 8. Material Properties of Seal Faces and Holder

Property	Carbon Face	Rotor (Tungsten Carbide)	Holder (17-4 PH Stainless Steel)
Elastic Modulus (10^{10} N/m^2)	2.4	63.0	19.6
Poisson's Ratio	0.25	0.20	0.30
Coeff. of Thermal Expansion (10^{-6}/C)	4.9	5.1	10.8
Thermal Conductivity (Watts/m C)	9.0	80.0	18.3
Density (kg/m^3)	1830	14,700	7750
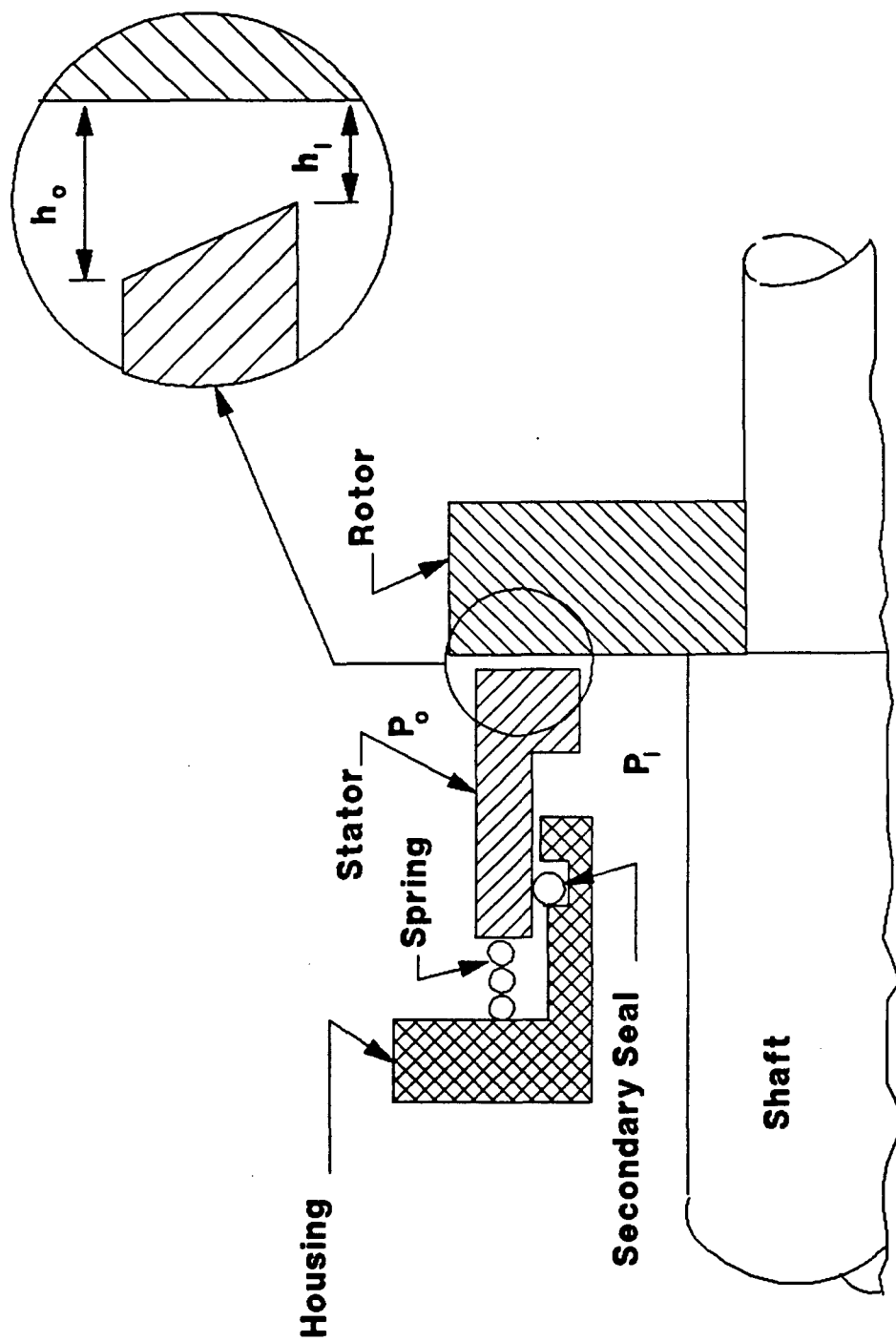
Figure 1. Diagram of a Mechanical Seal
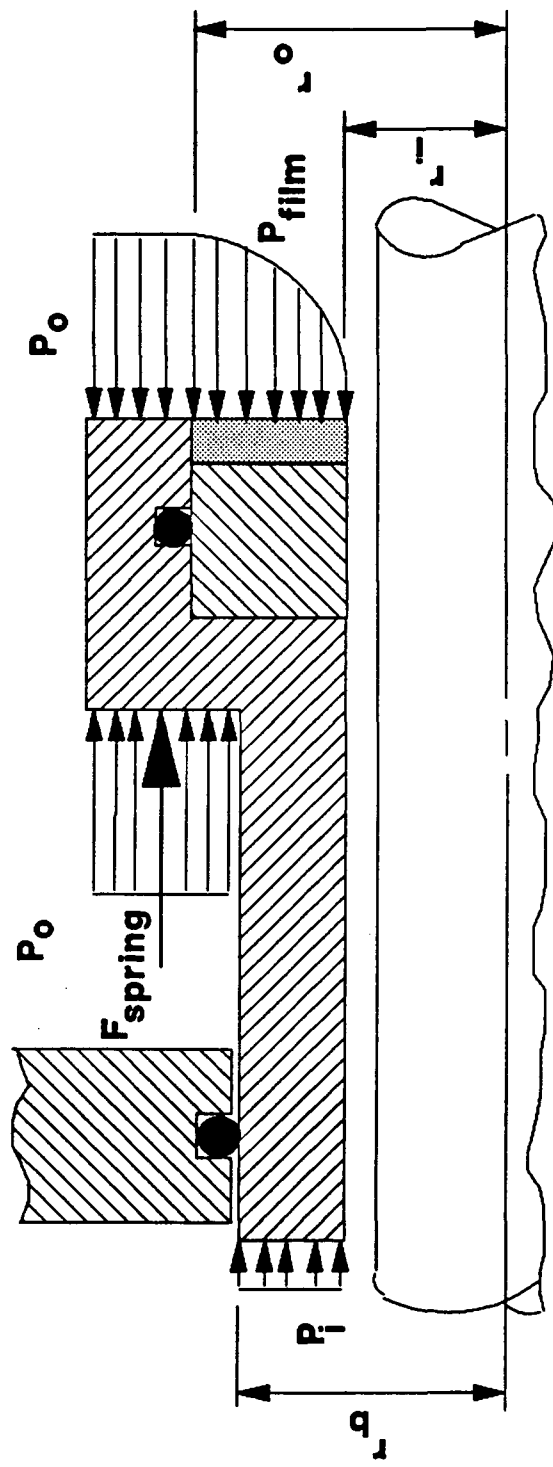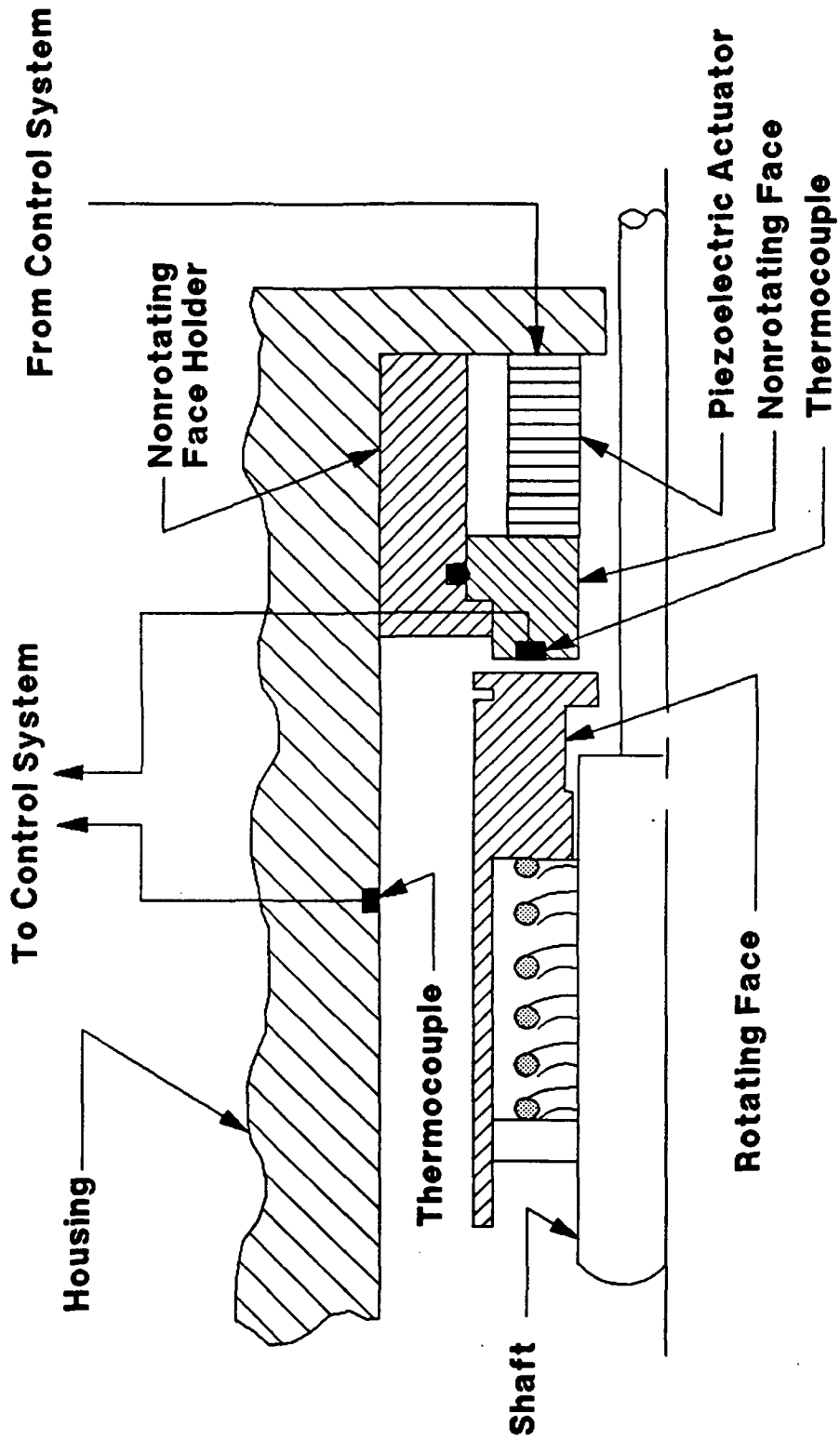
Figure 2. Forces Acting on Floating Component

From Control System

Nonrotating Face Holder

Piezoelectric Actuator

Nonrotating Face

Thermocouple

To Control System

Housing

Thermocouple

Shaft

Rotating Face

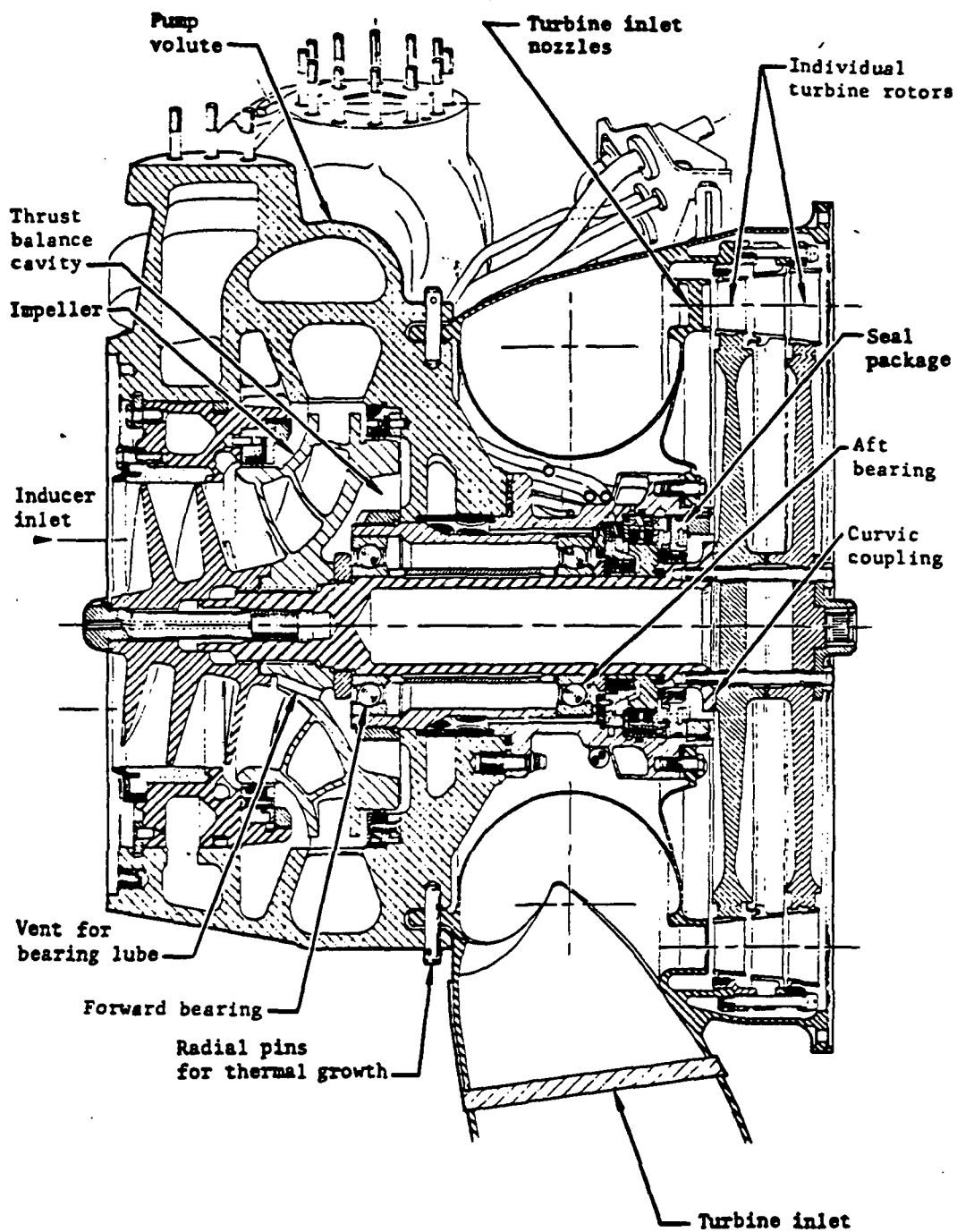**Figure 3. Actively Controlled Seal for Industrial Use**

C-2

Figure 4. Schematic of a Typical Turbopump
From Sobin and Bissel [1974]

87

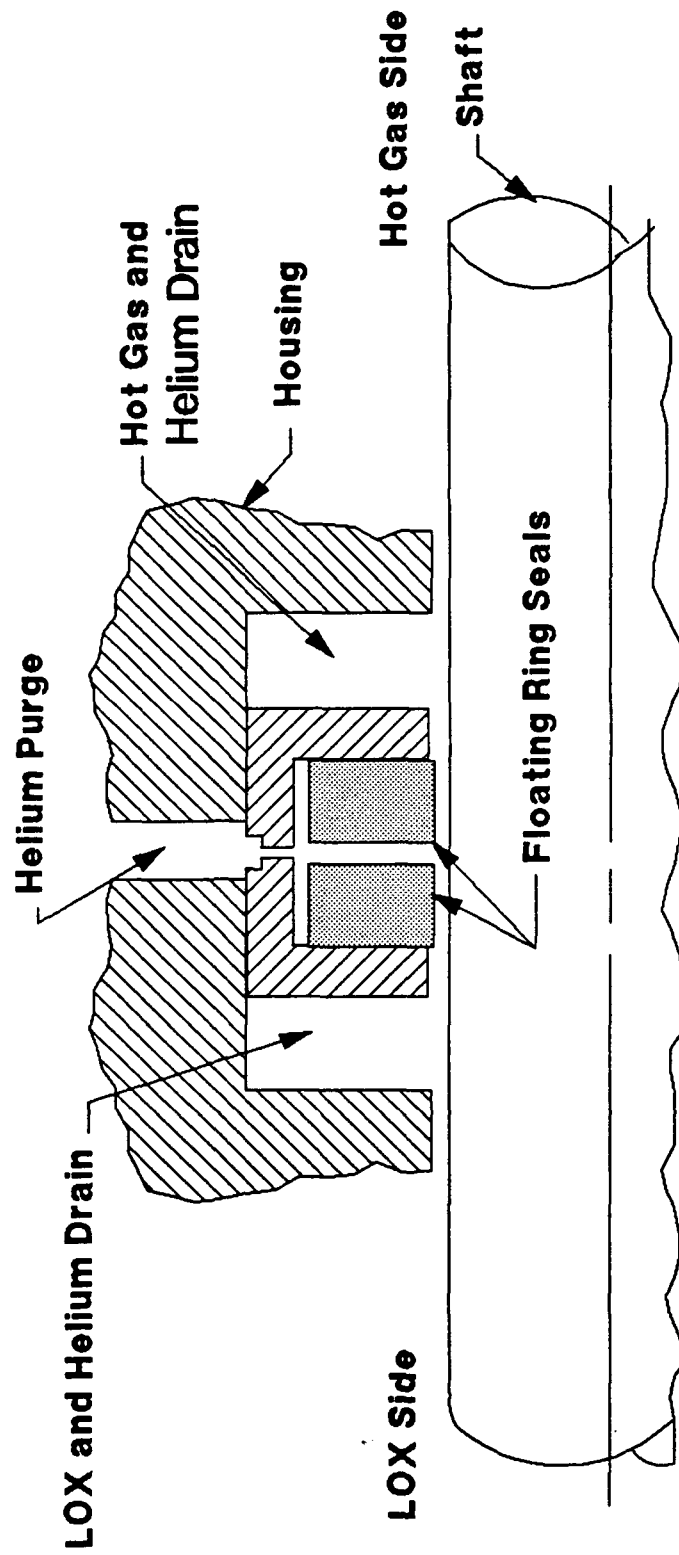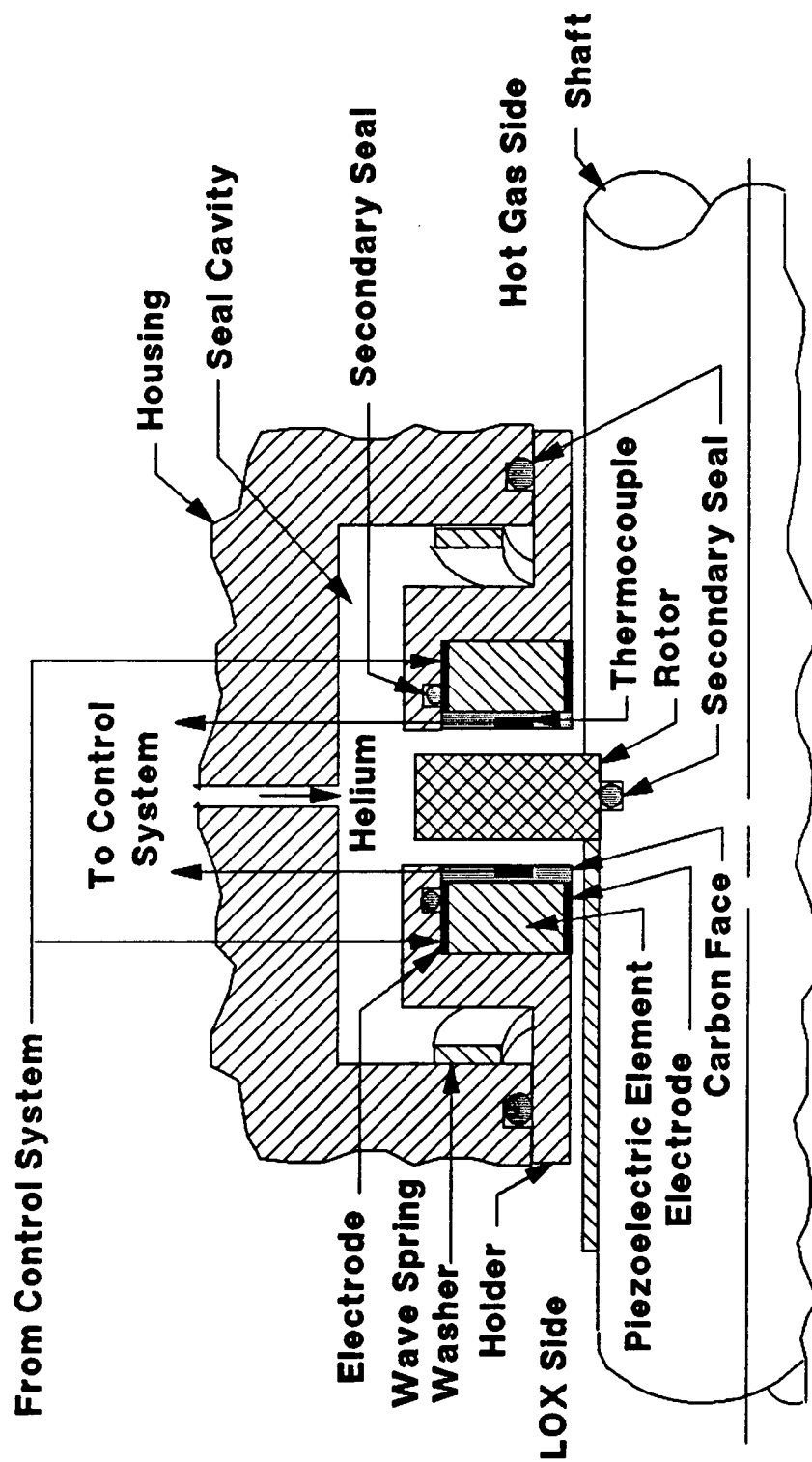**Figure 5. Helium Purge Assembly**

Figure 6. Proposed Seal Design
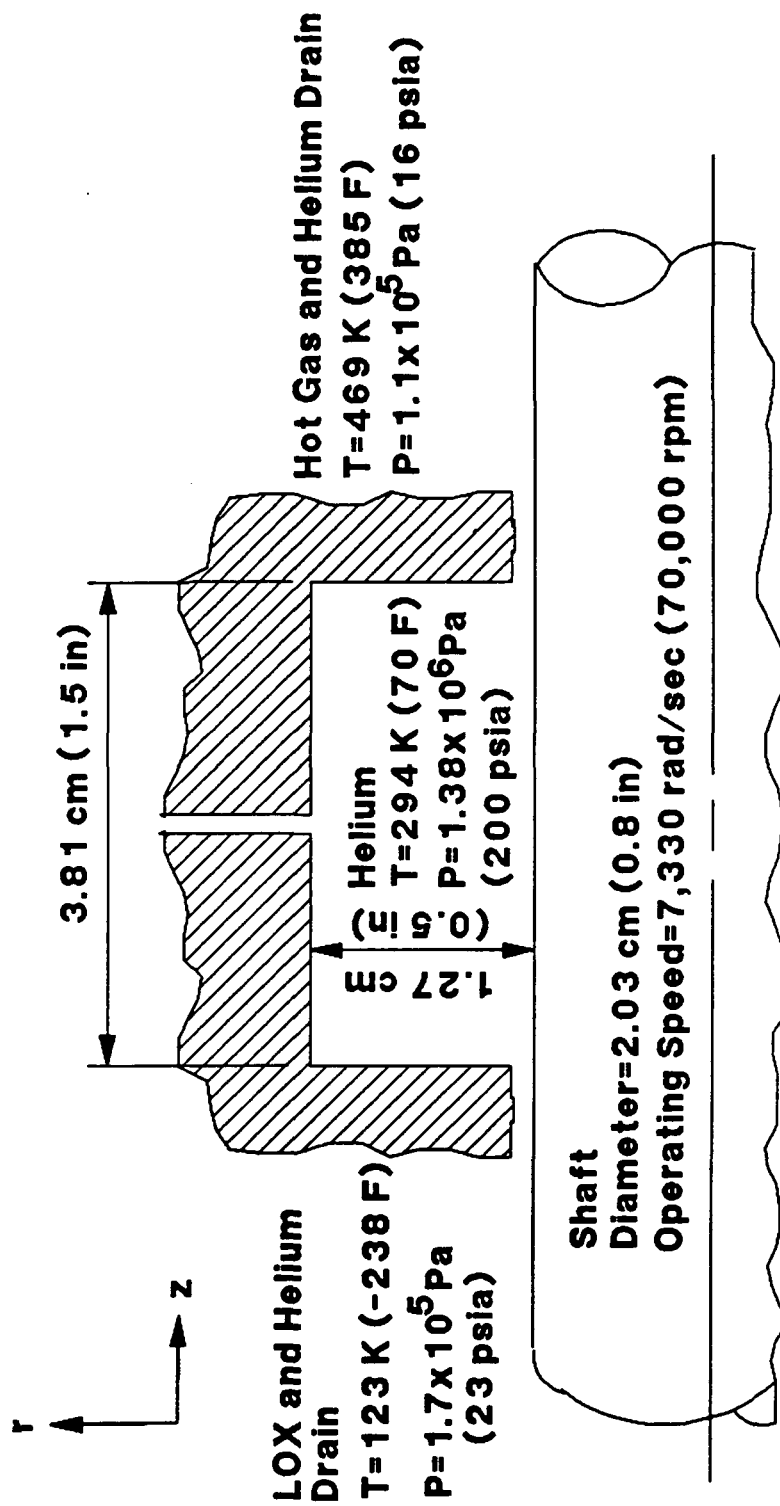
Hot Gas and Helium Drain
T=469 K (385 F)
P=1.1x10^5 Pa (16 psia)

3.81 cm (1.5 in)

Helium
T=294 K (70 F)
P=1.38x10^{6}Pa
(200 psia)

1.27 cm (0.5 in)

LOX and Helium Drain
T=123 K (-238 F)
P=1.7x10^{5}Pa
(23 psia)

z

r

Shaft
Diameter=2.03 cm (0.8 in)
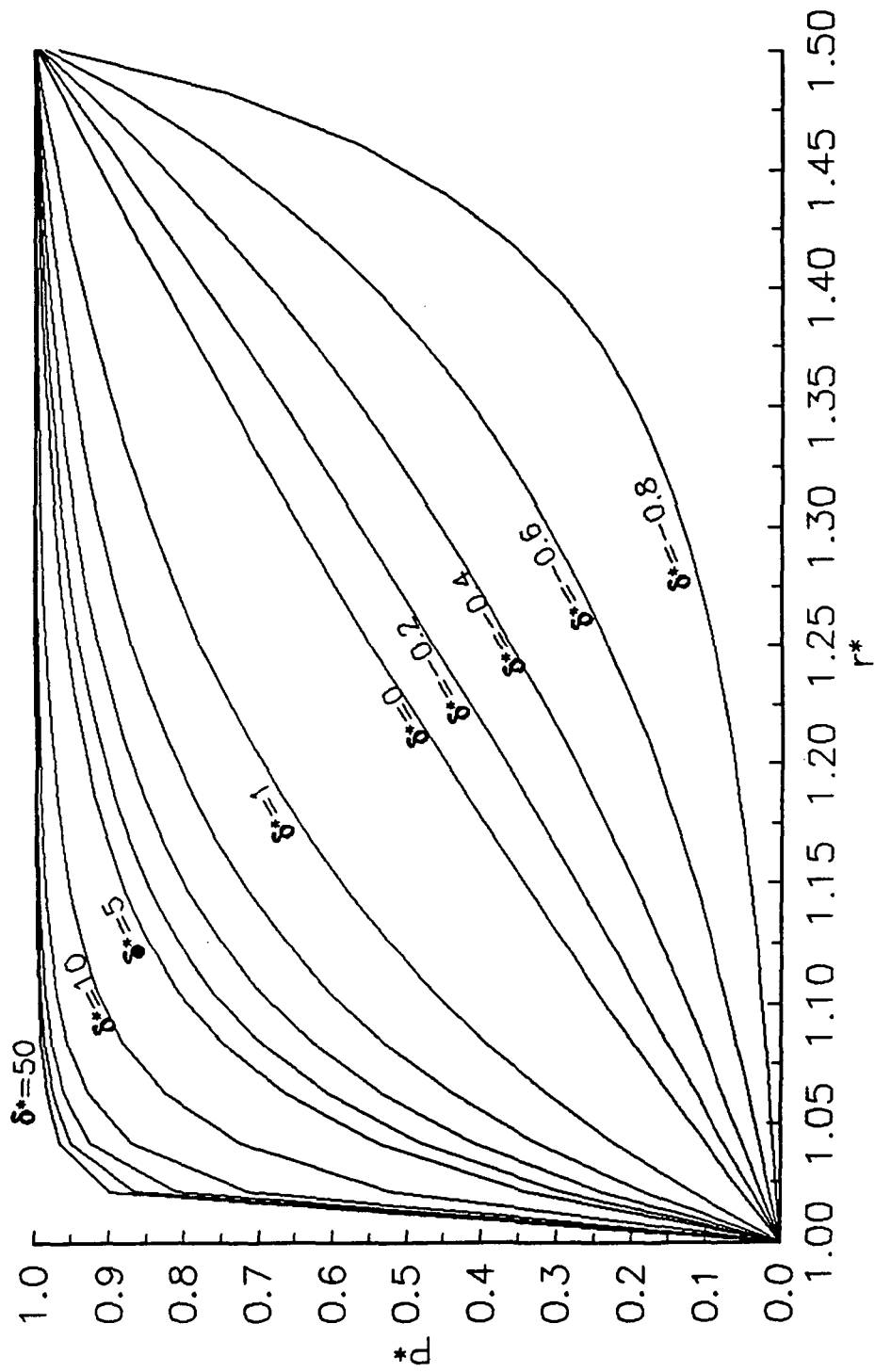Operating Speed=7,330 rad/sec (70,000 rpm)

Figure 7. Design Constraints

Figure 8. Nondimensional Pressure Distribution
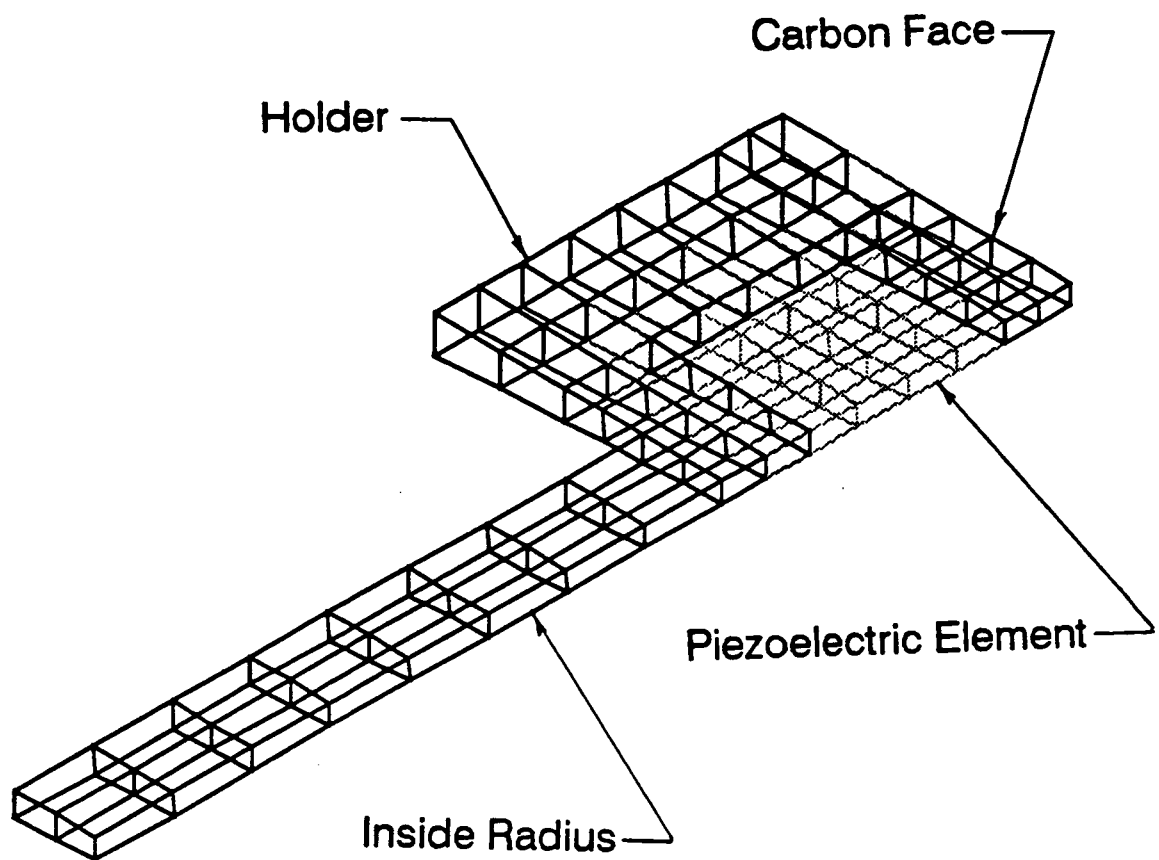
Figure 9. Finite Element Model of Floating Component
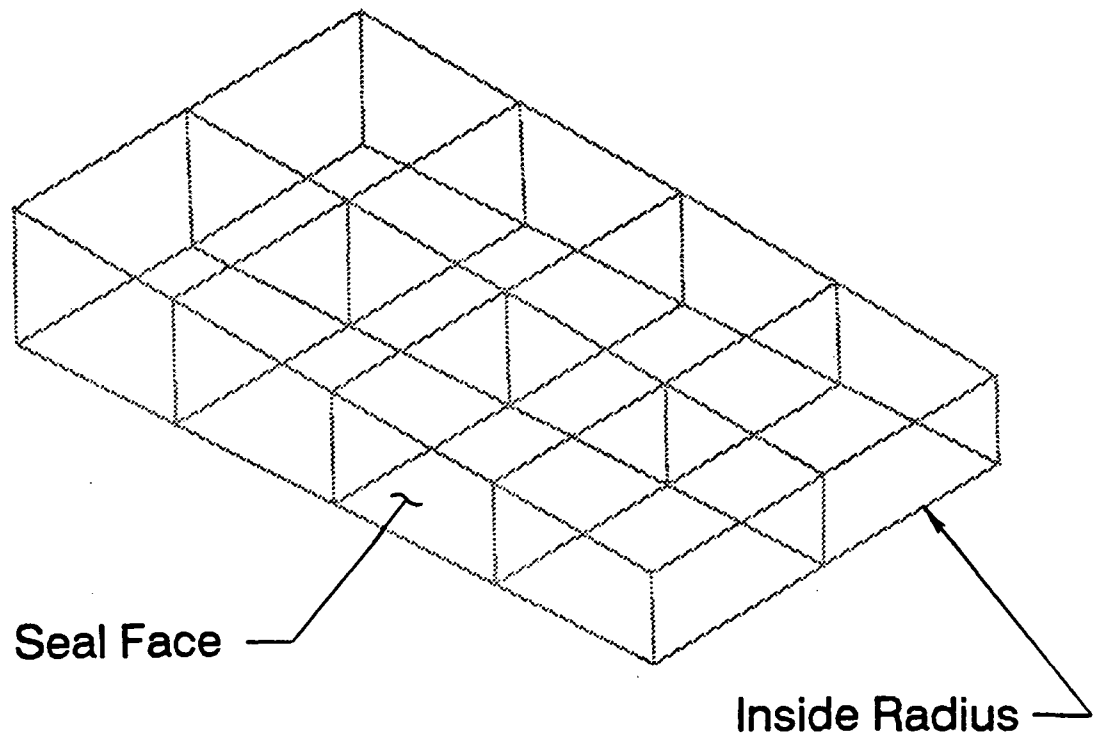
Seal Face

Inside Radius

Figure 10. Finite Element Model of Rotor

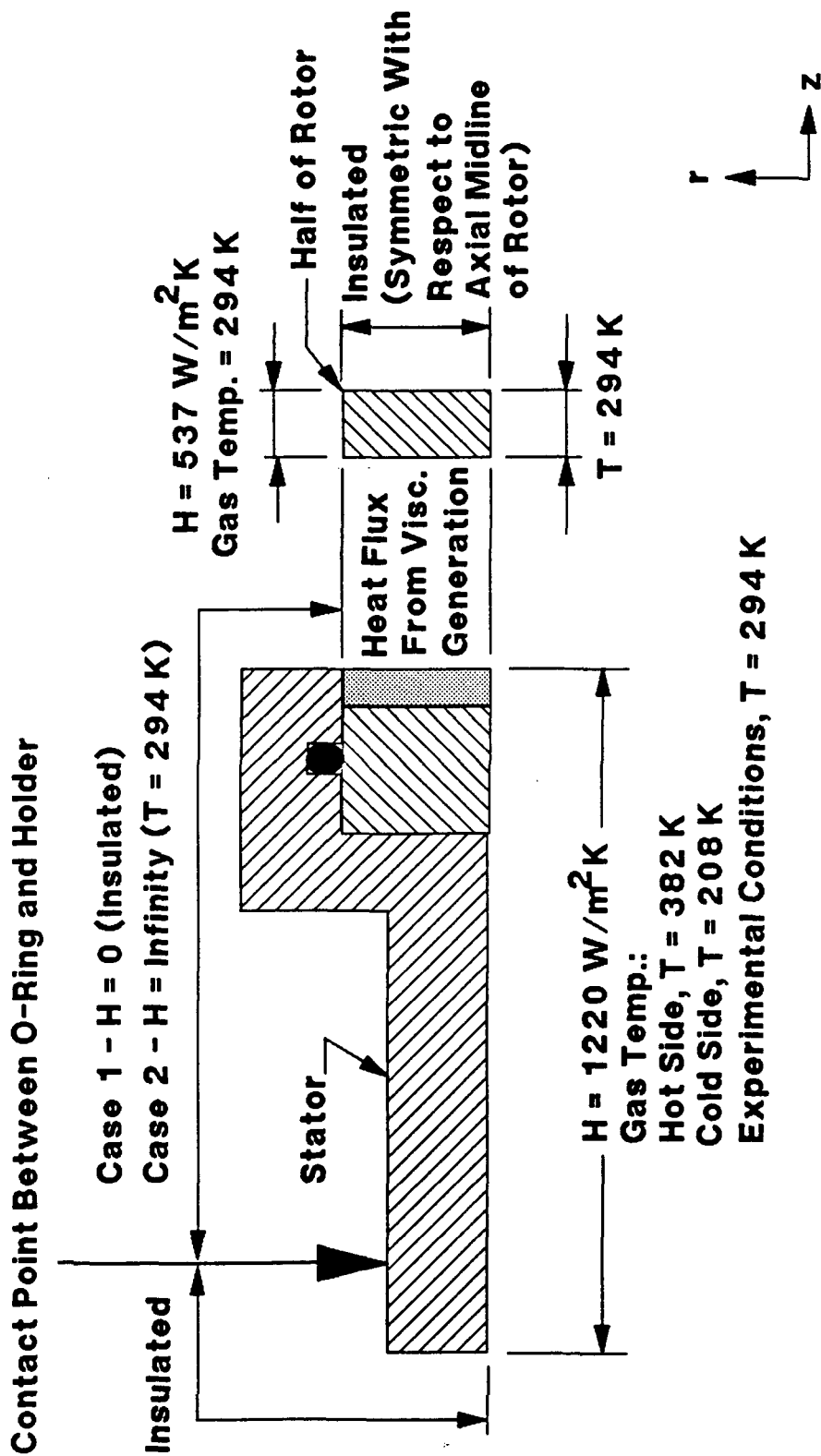**Figure 11. Thermal Boundary Conditions**
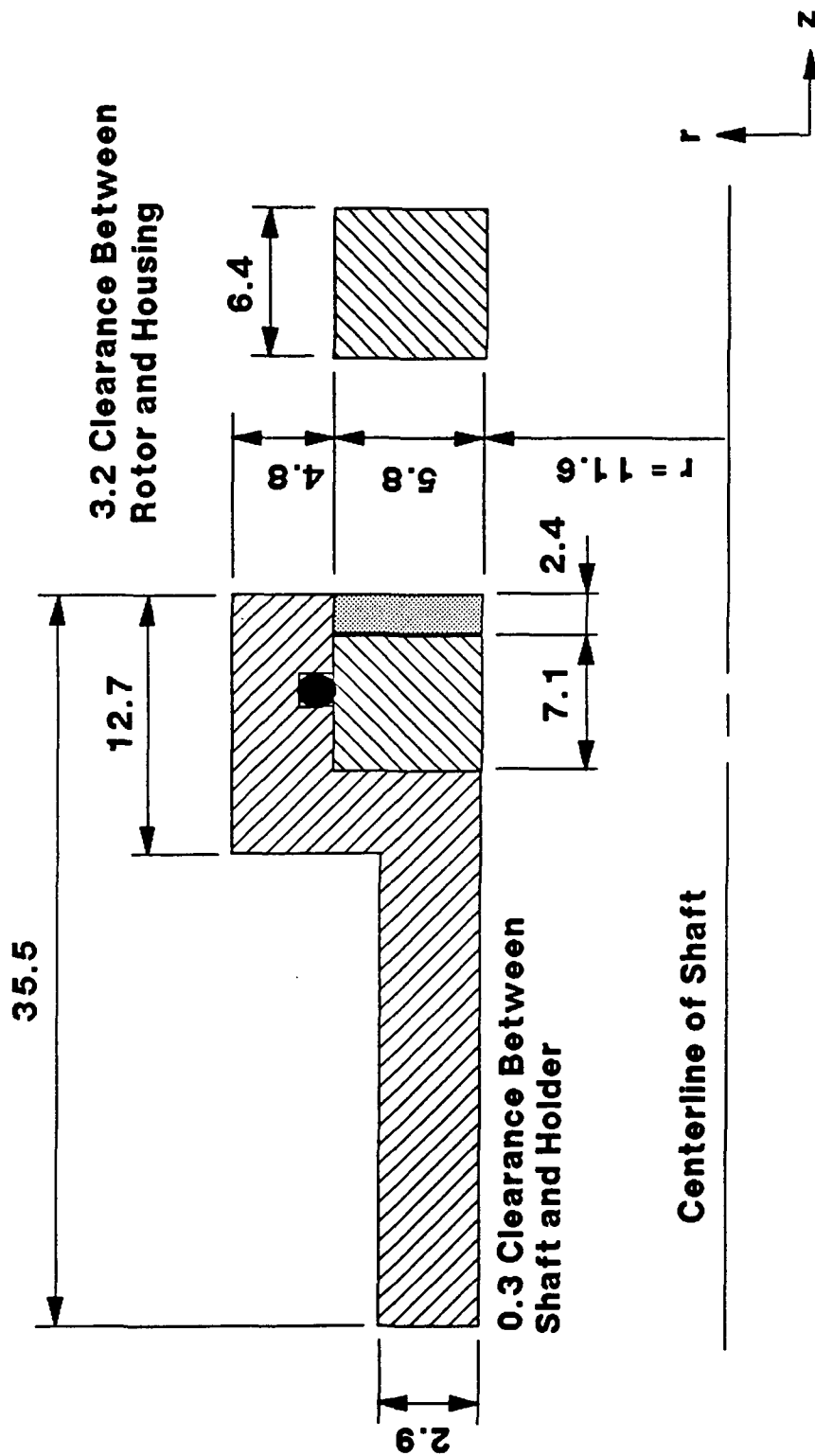
Figure 12. Preliminary Design Dimensions
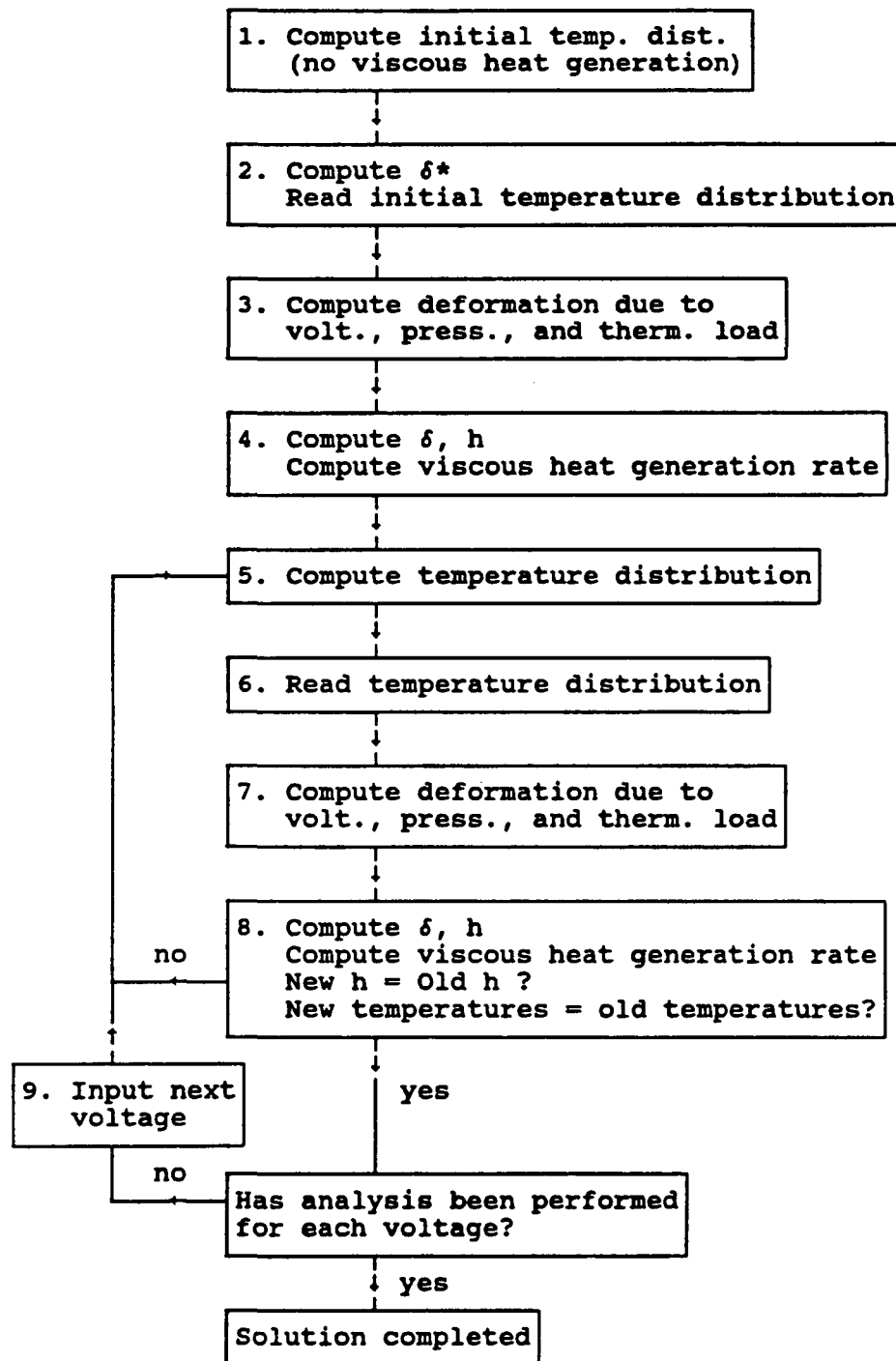
All Dimensions in Millimeters
N.T.S.

3.2 Clearance Between
Rotor and Housing

0.3 Clearance Between
Shaft and Holder

Centerline of Shaft

6.4

4.8

5.8

r = 11.6

2.4

7.1

12.7

35.5

2.9

r

z

```
┌─────────────────────────────────────┐
│ 1. Compute initial temp. dist.      │
│    (no viscous heat generation)     │
└─────────────────────────────────────┘
                    │
┌─────────────────────────────────────────┐
│ 2. Compute δ*                           │
│    Read initial temperature distribution │
└─────────────────────────────────────────┘
                    │
┌─────────────────────────────────────┐
│ 3. Compute deformation due to       │
│    volt., press., and therm. load   │
└─────────────────────────────────────┘
                    │
┌─────────────────────────────────────────┐
│ 4. Compute δ, h                         │
│    Compute viscous heat generation rate │
└─────────────────────────────────────────┘
                    │
┌─────────────────────────────────────┐
│ 5. Compute temperature distribution │
└─────────────────────────────────────┘
                    │
┌─────────────────────────────────────┐
│ 6. Read temperature distribution    │
└─────────────────────────────────────┘
                    │
┌─────────────────────────────────────┐
│ 7. Compute deformation due to       │
│    volt., press., and therm. load   │
└─────────────────────────────────────┘
                    │
┌──────────────────────────────────────────┐
│ 8. Compute δ, h                          │
│    Compute viscous heat generation rate  │
│    New h = Old h ?                       │
│    New temperatures = old temperatures?  │
└──────────────────────────────────────────┘
          no                    │
┌────────────────┐           yes │
│ 9. Input next  │               │
│    voltage     │               │
└────────────────┘               │
          no                     │
┌──────────────────────────────────┐
│ Has analysis been performed      │
│ for each voltage?                │
└──────────────────────────────────┘
                    │ yes
┌──────────────────────┐
│ Solution completed   │
└──────────────────────┘
```

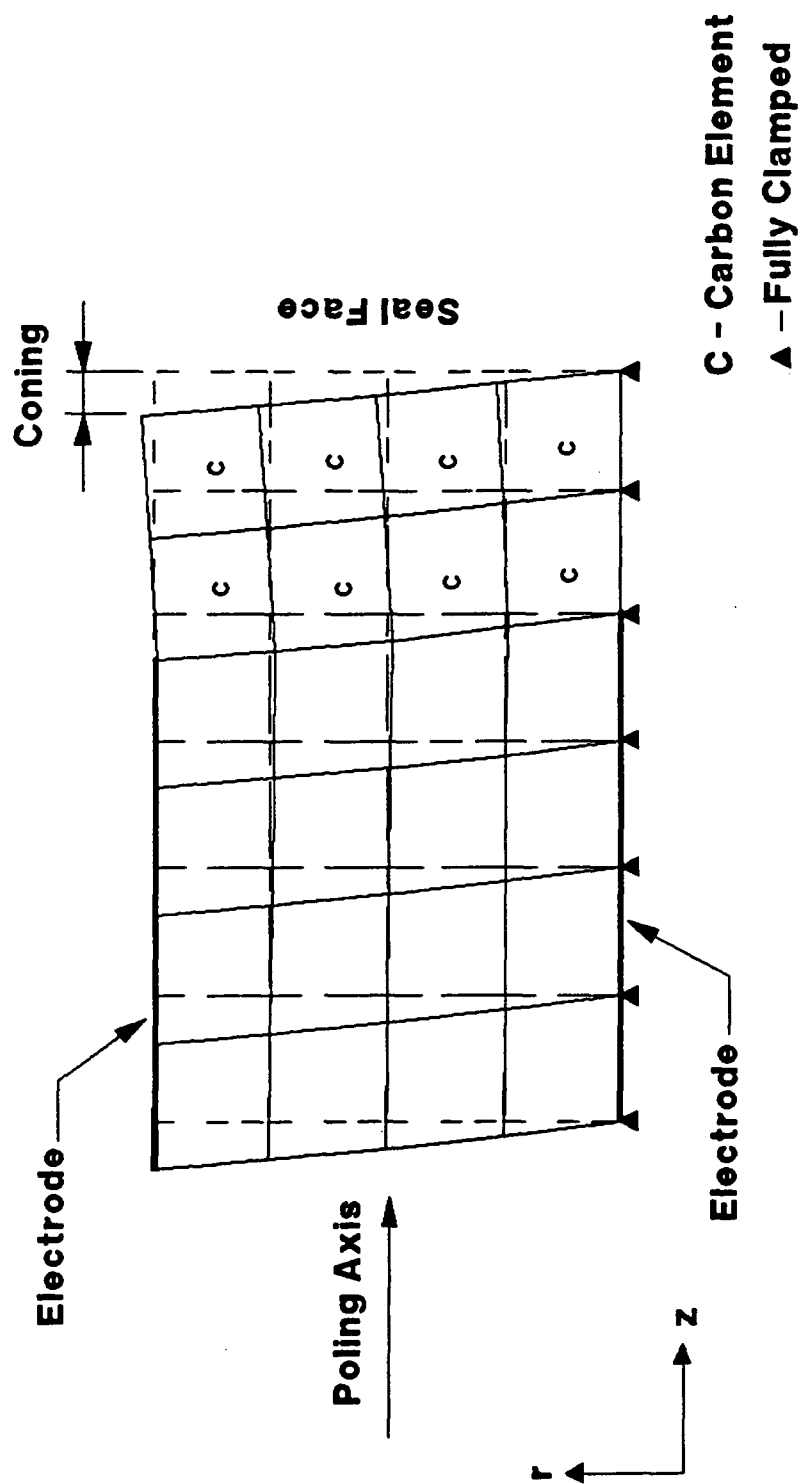Figure 13. Computational Procedure

96

Figure 14. Shear Mode
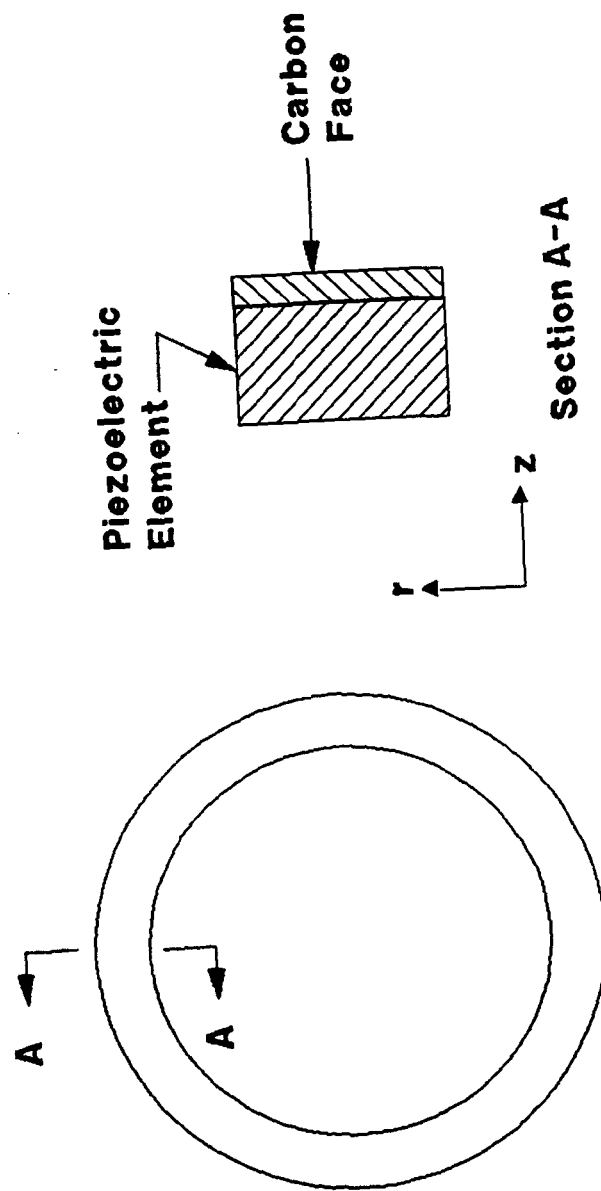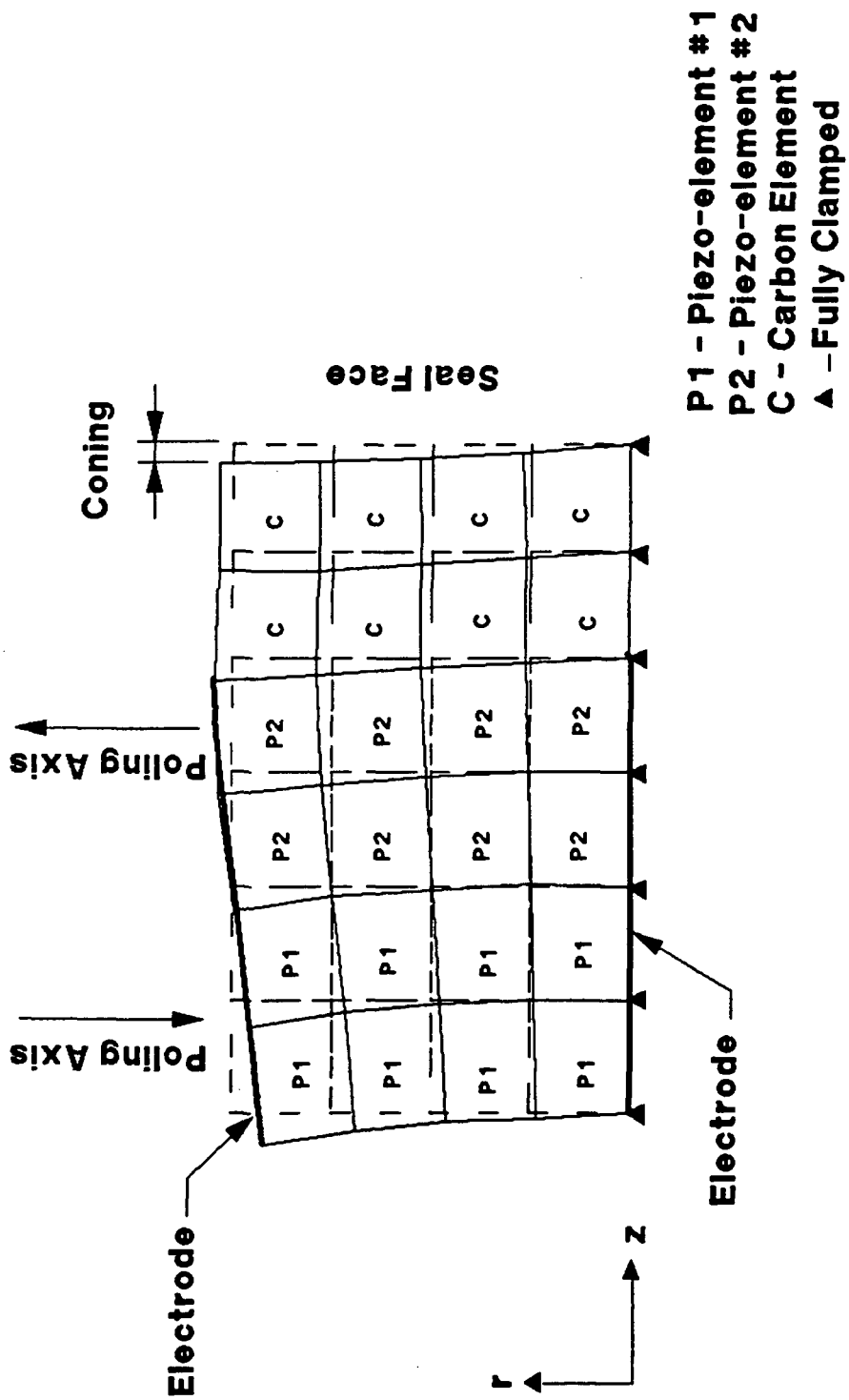
Figure 15. Schematic of Deformable Face Assembly

Figure 16. Bimorph

P1 – Piezo-element #1
P2 – Piezo-element #2
C – Carbon Element
▲ –Fully Clamped

C – Carbon Element
▲ – Fully Clamped
⚙ – Constrained in z-direction
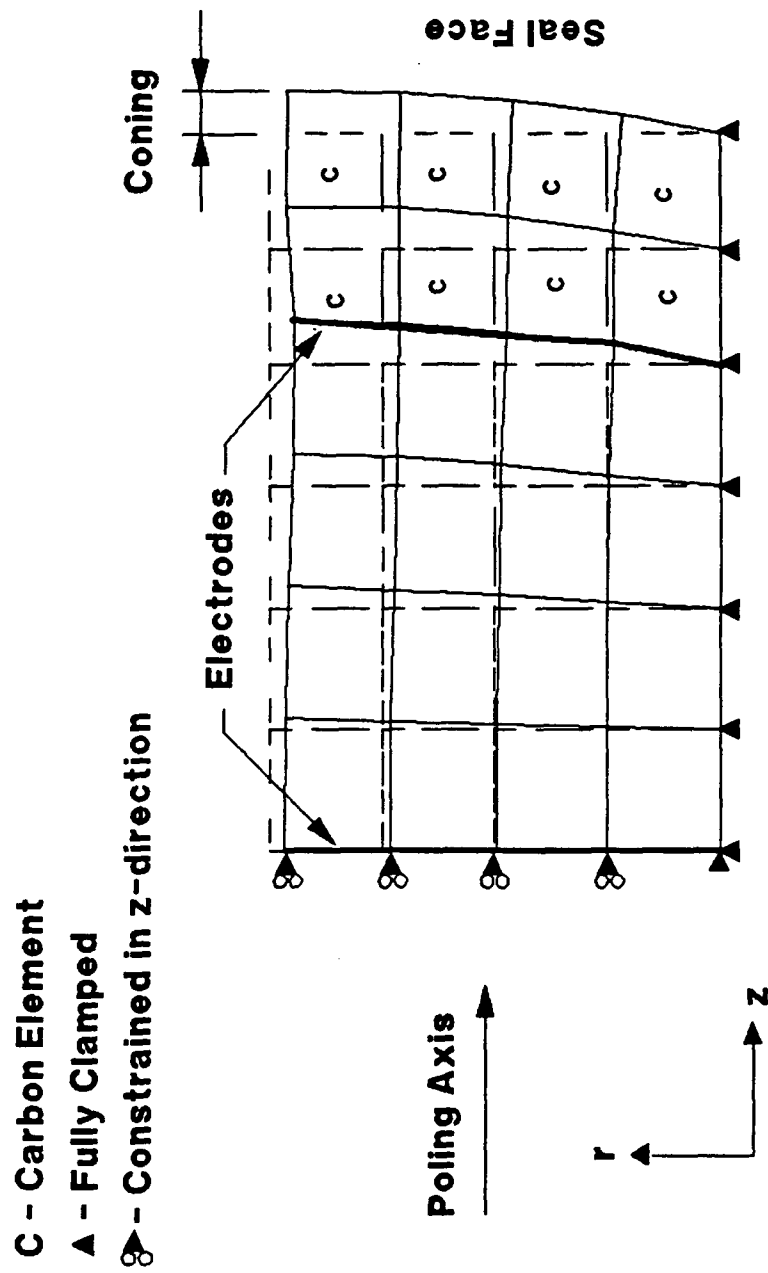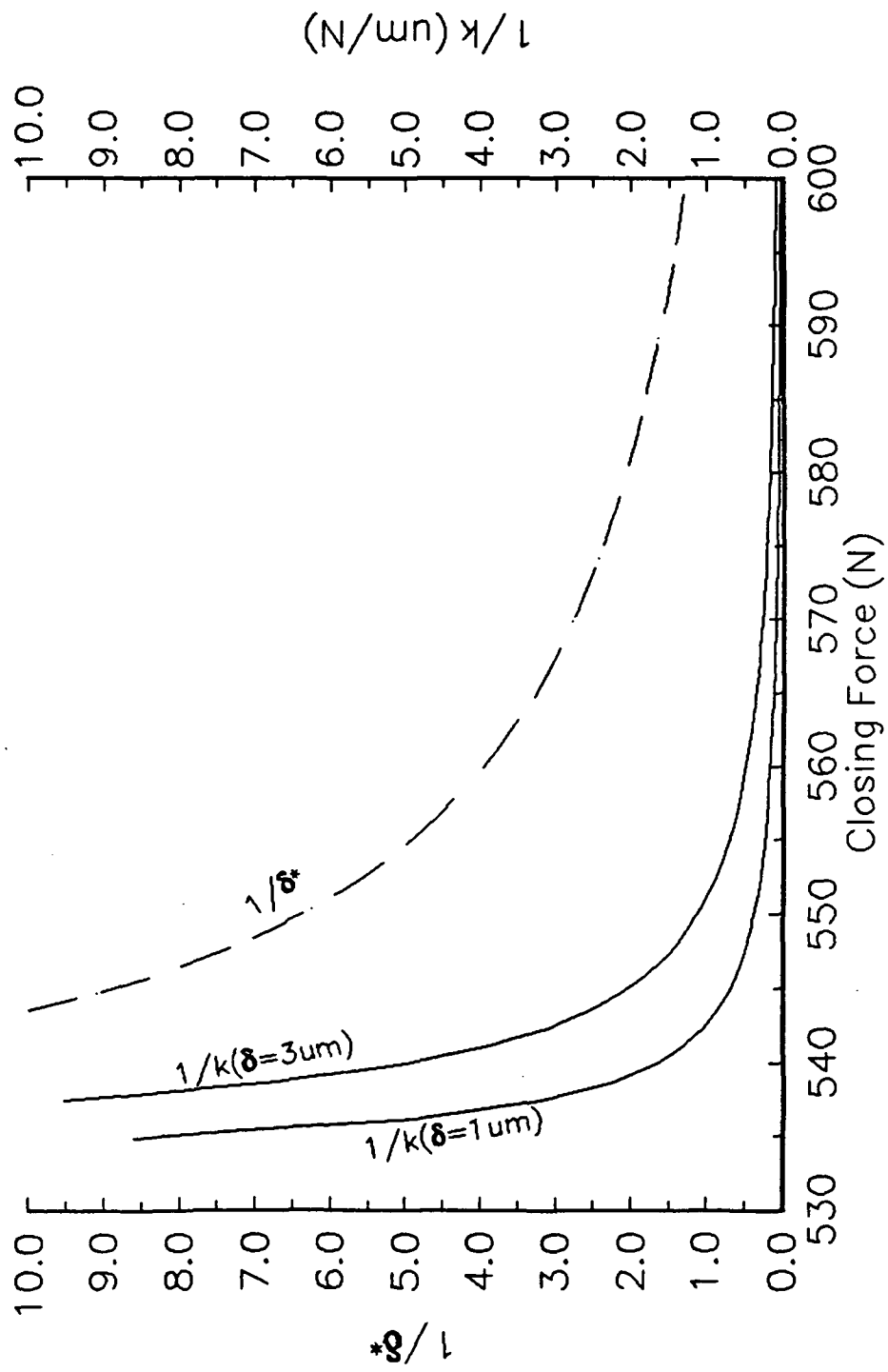
Poling Axis

z

r

Figure 17. Axial Mode

Figure 18. Effect of Closing Force on Controllability and Stability

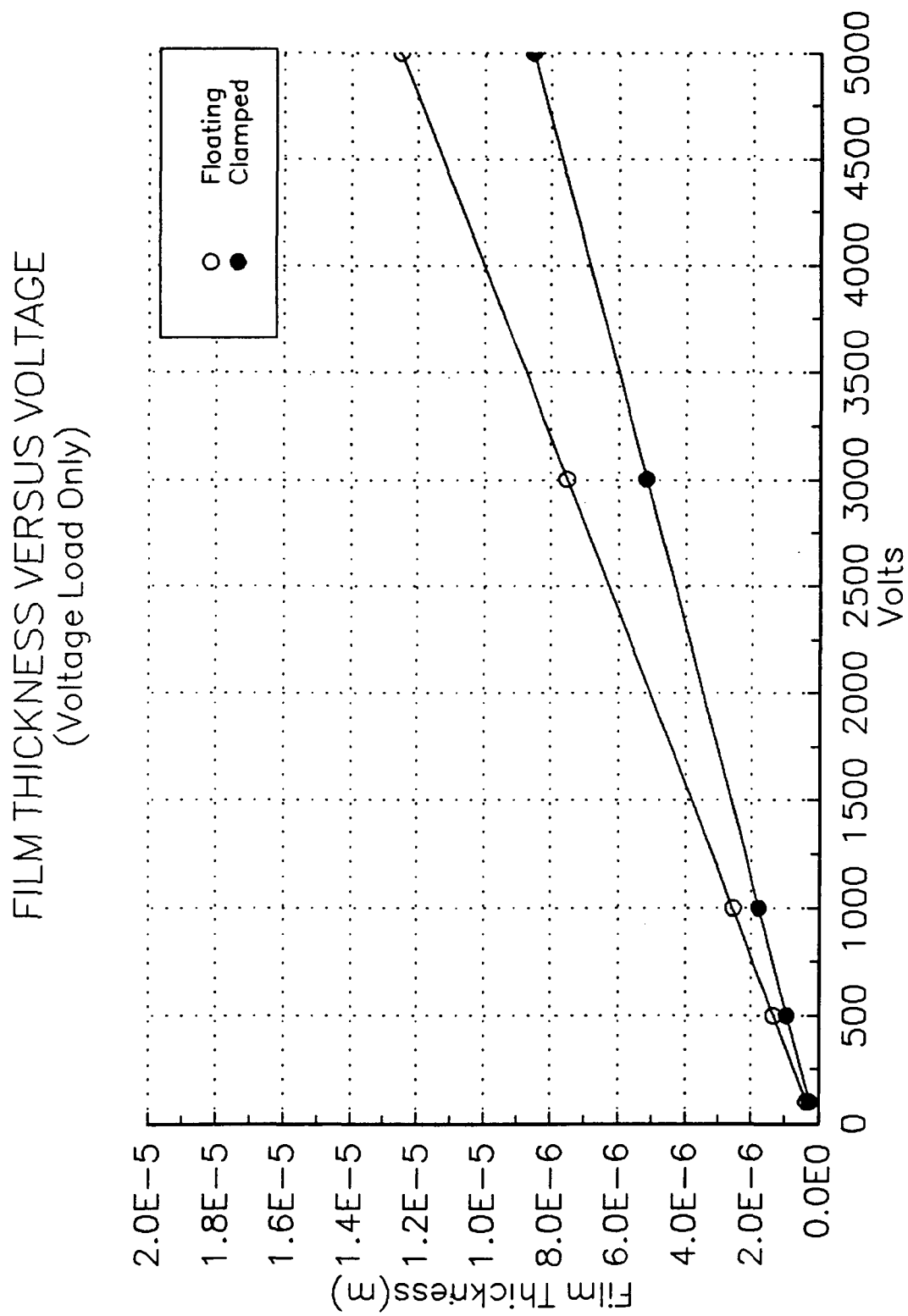Figure 19. Comparison of Boundary Conditions
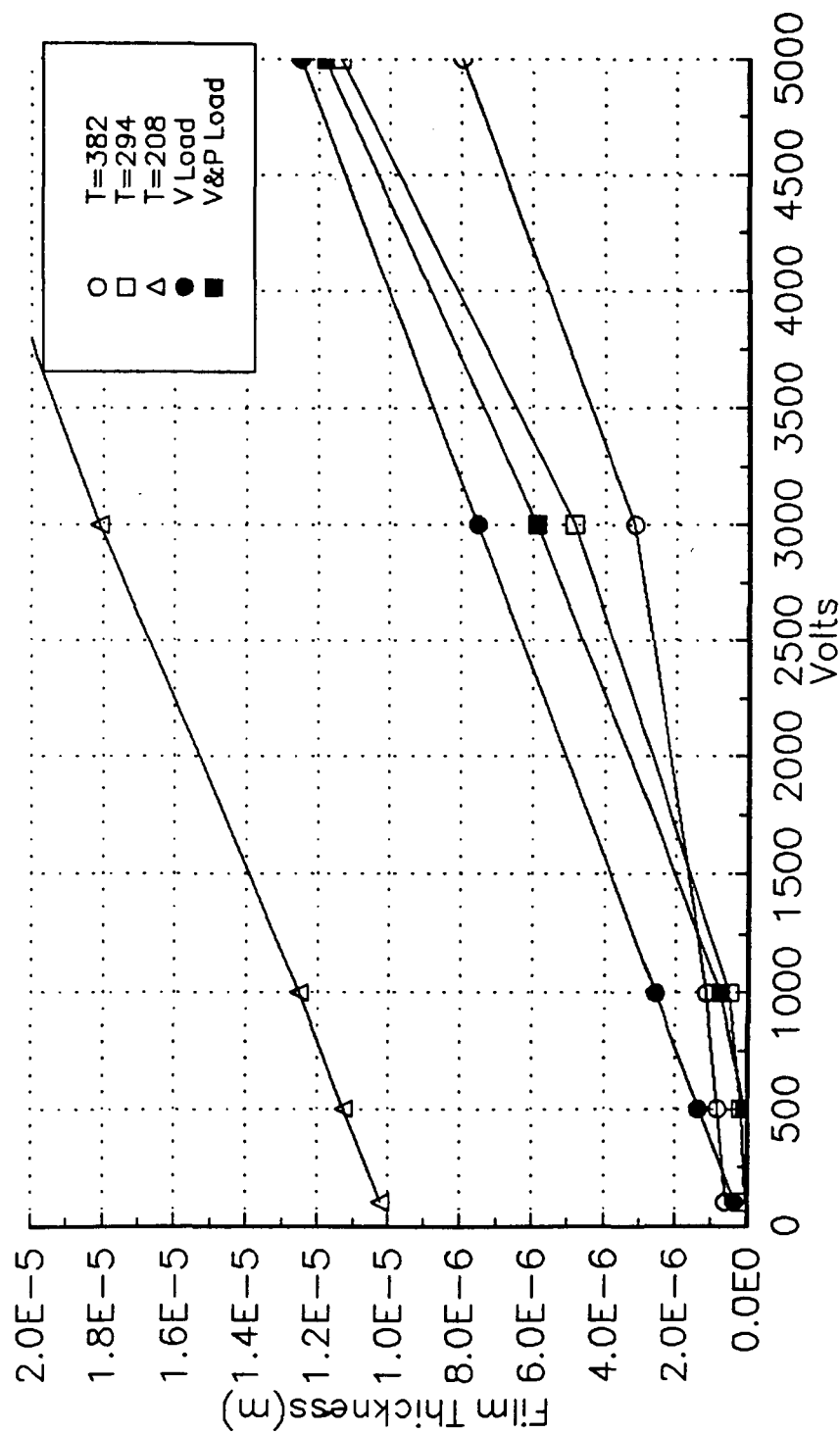
FILM THICKNESS VERSUS VOLTAGE

Figure 20. Seal Performance – Insulated at Outside Radius

103
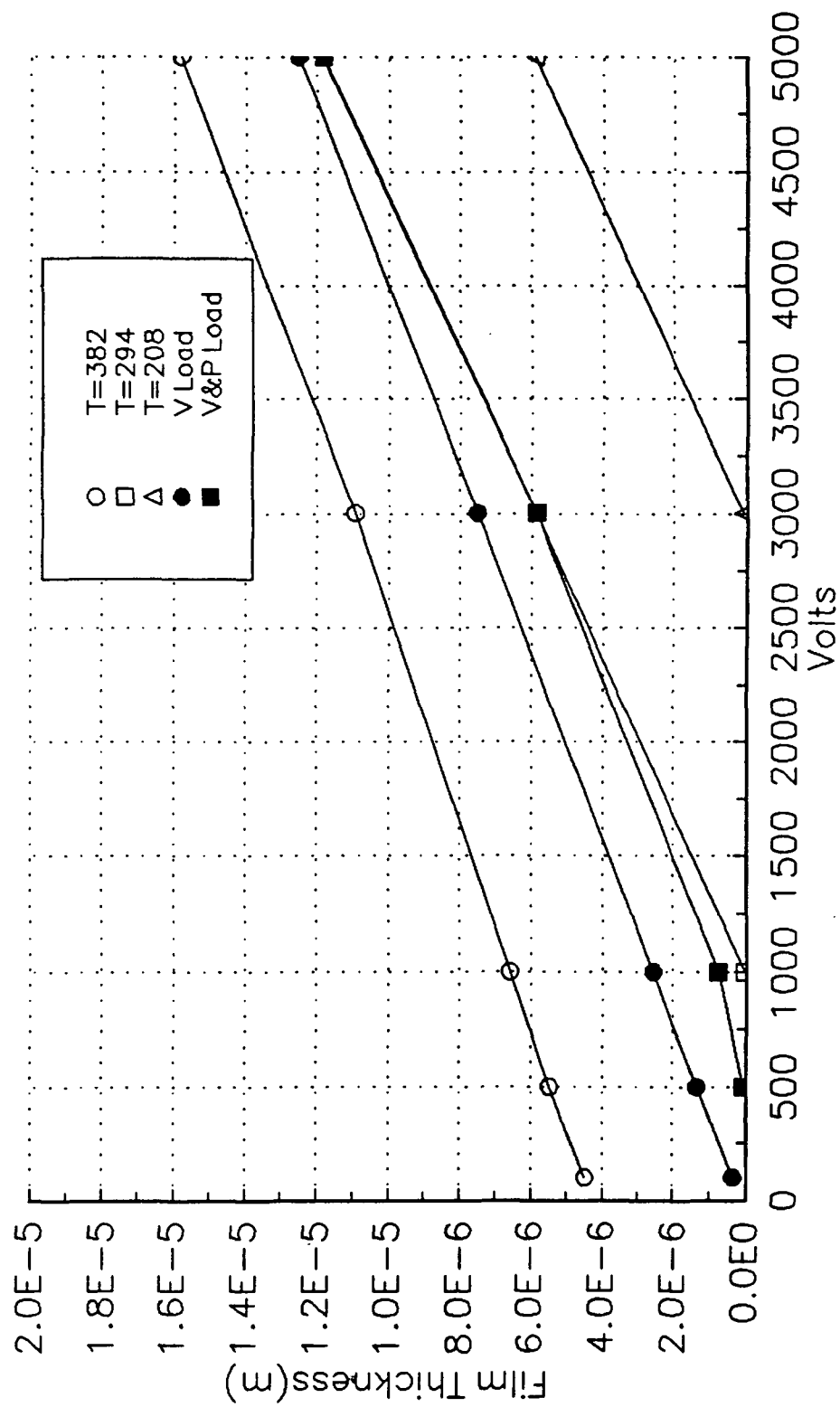
Figure 21. Seal Performance — T=294 K at Outside Radius of Holder
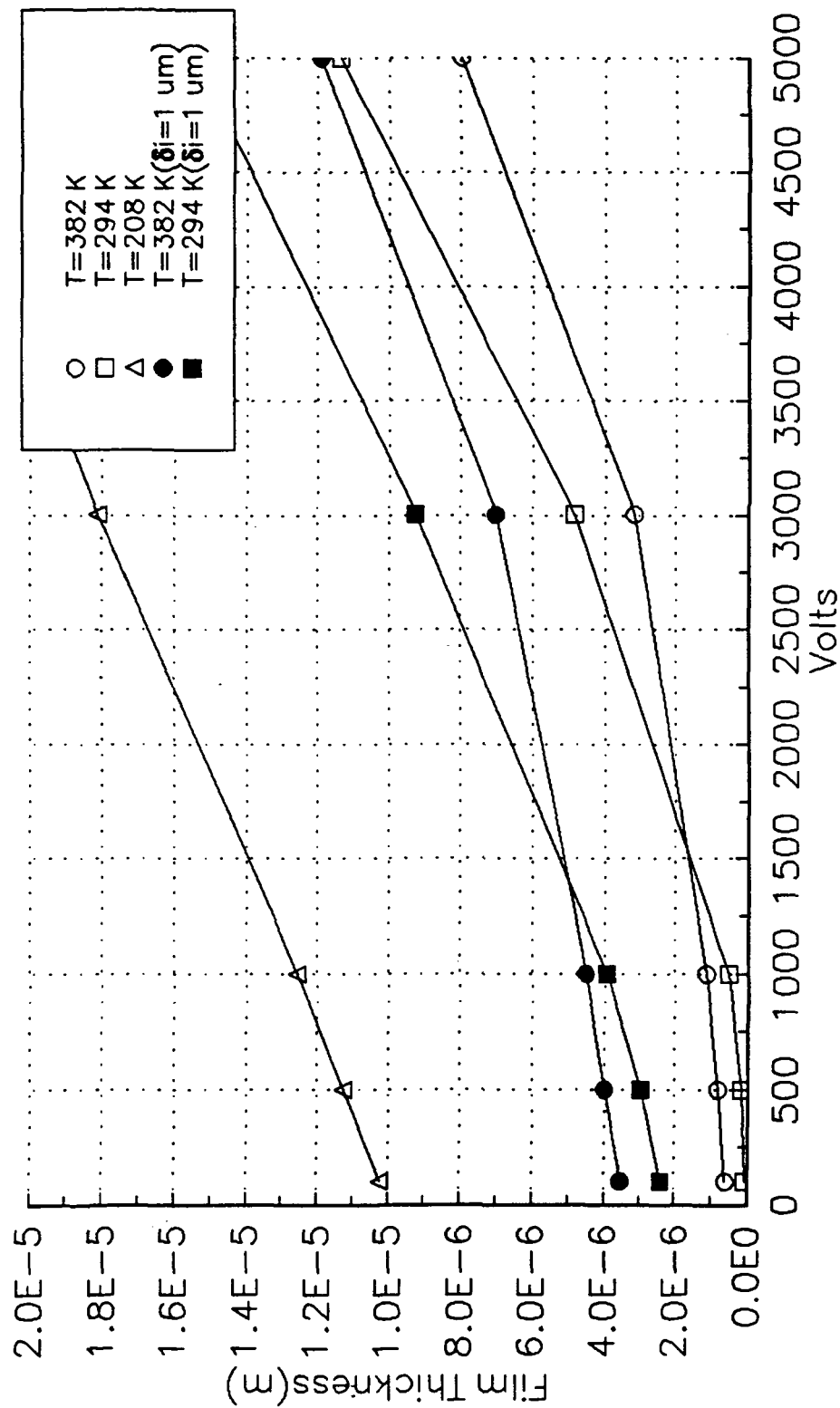
Figure 22. Seal Performance — Effects of Initial Coning

LEAKAGE VERSUS VOLTAGE
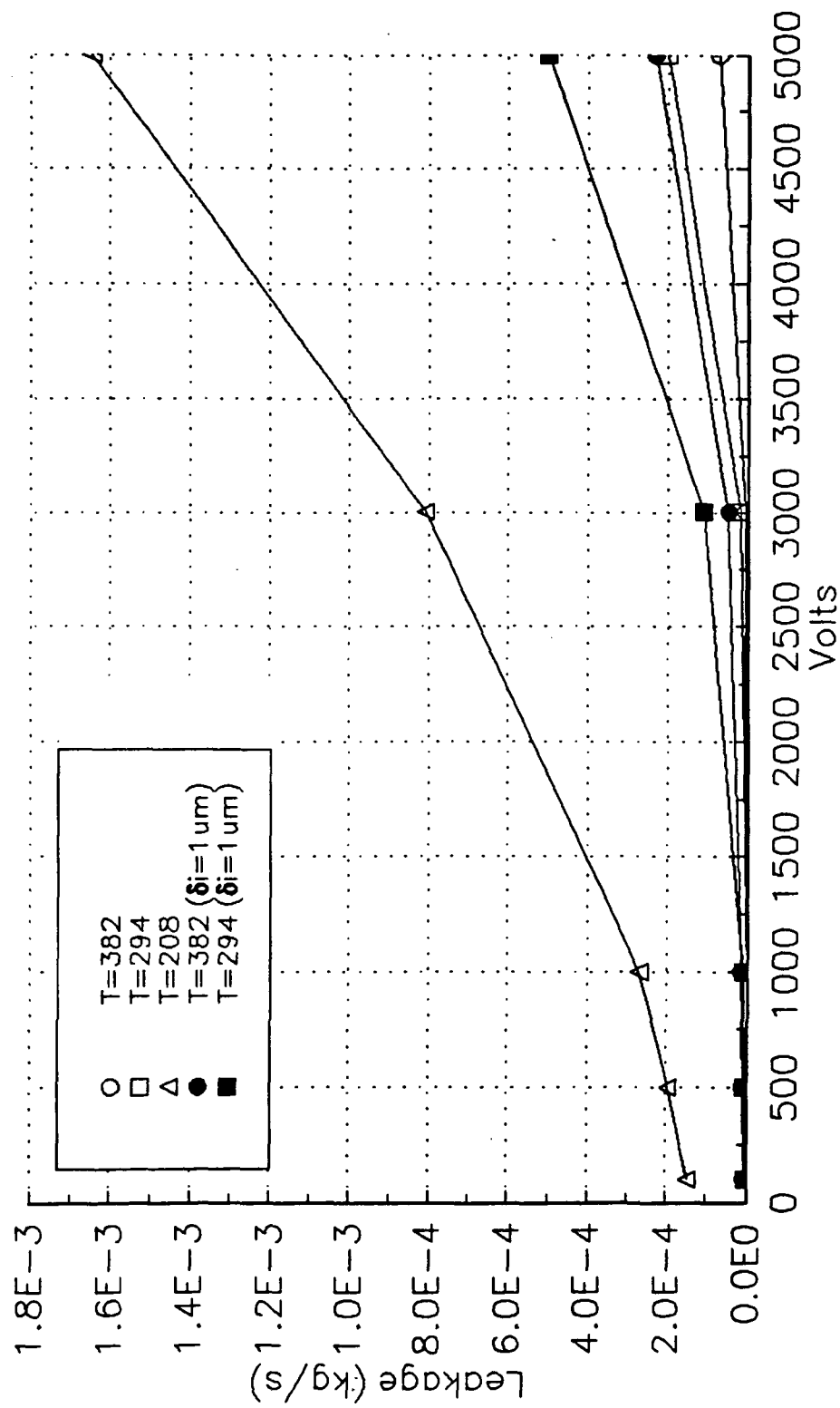(Insulated at Outside Radius of Holder)

Figure 23. Seal Performance — Leakage
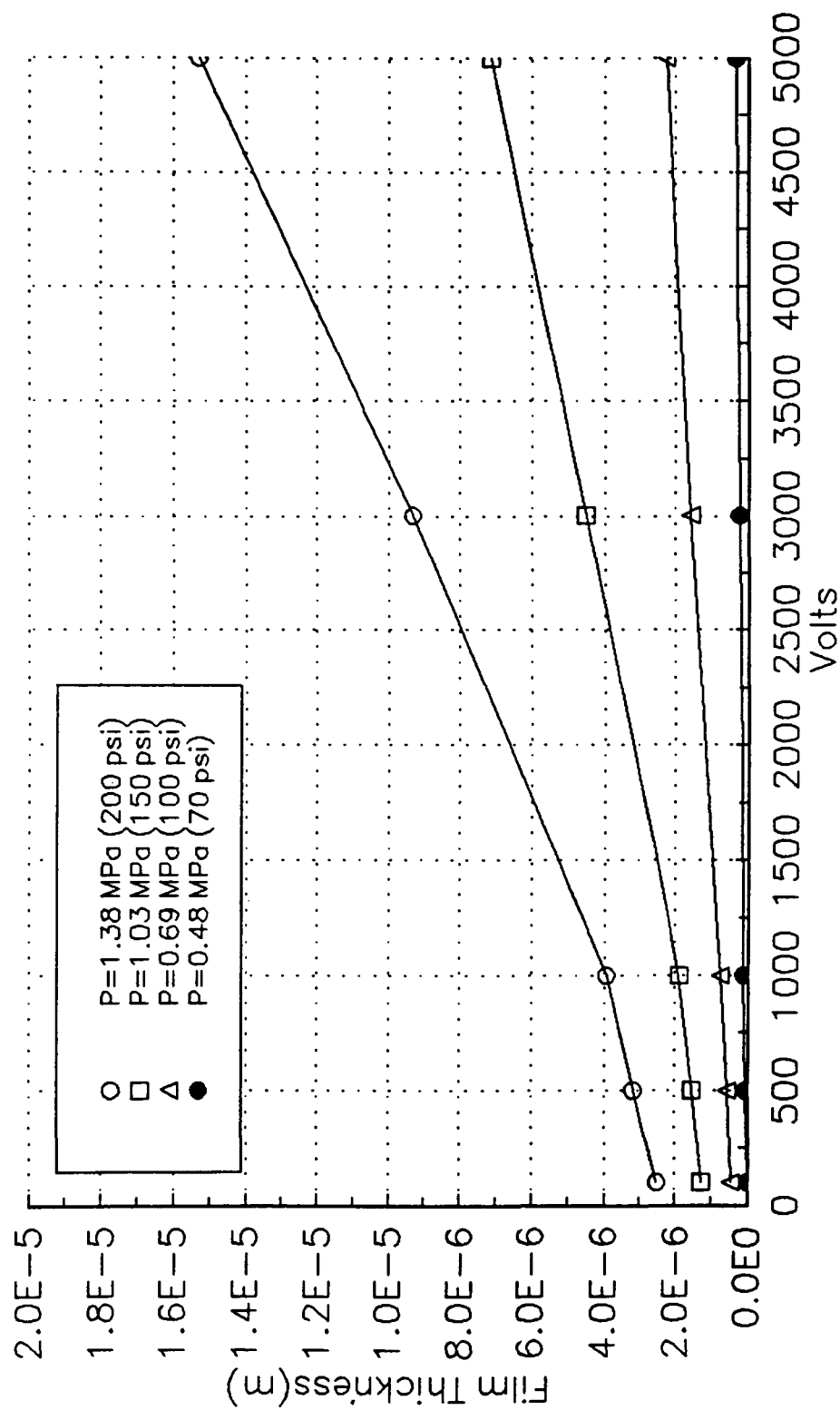
FILM THICKNESS VERSUS VOLTAGE

Figure 24. Seal Performance – Variable Pressure Operation

FILM THICKNESS VERSUS VOLTAGE
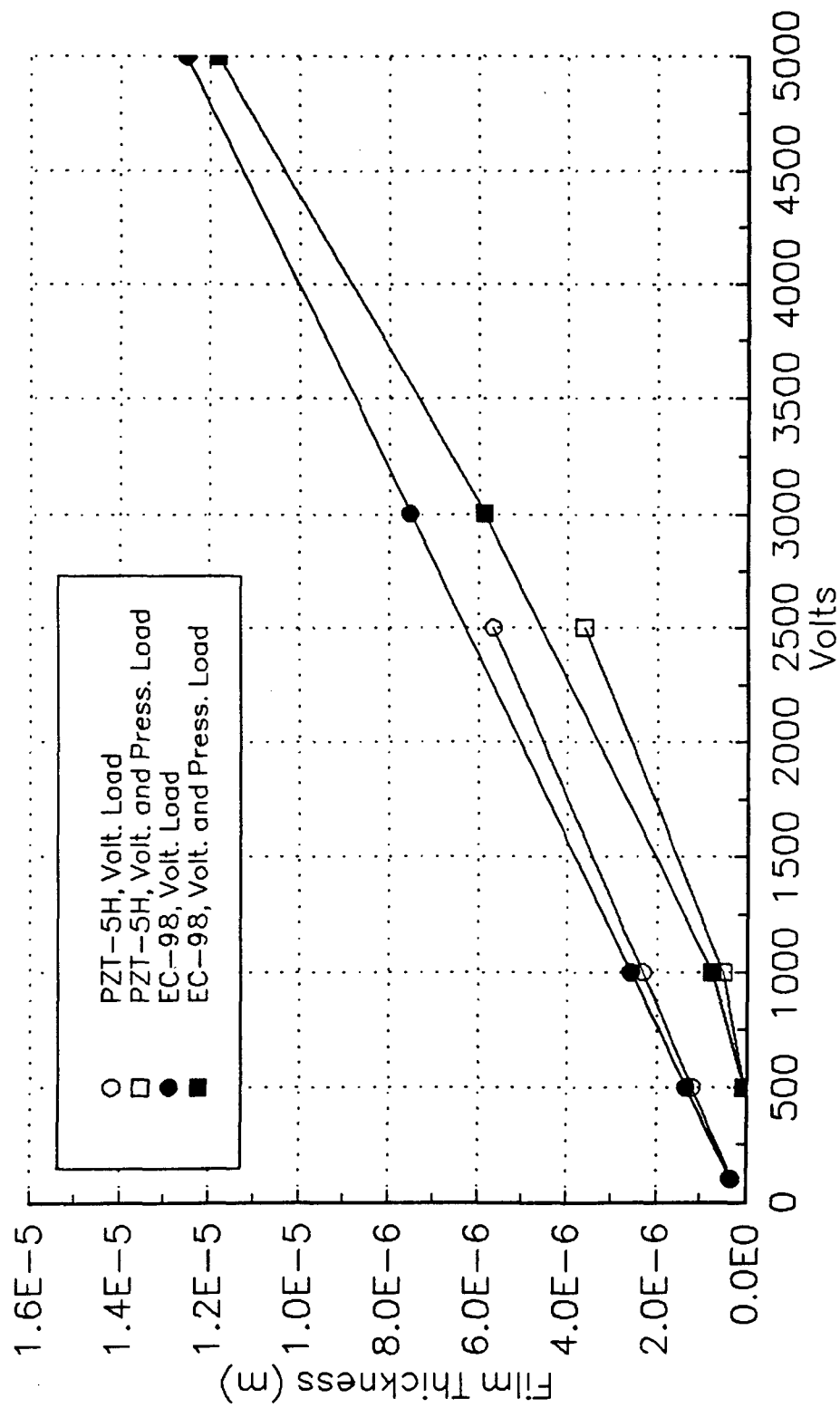(Comparison of PZT-5H and EC-98)

Figure 25. Seal Performance — Comparison of Piezoelectric Materials

FILM THICKNESS VERSUS VOLTAGE
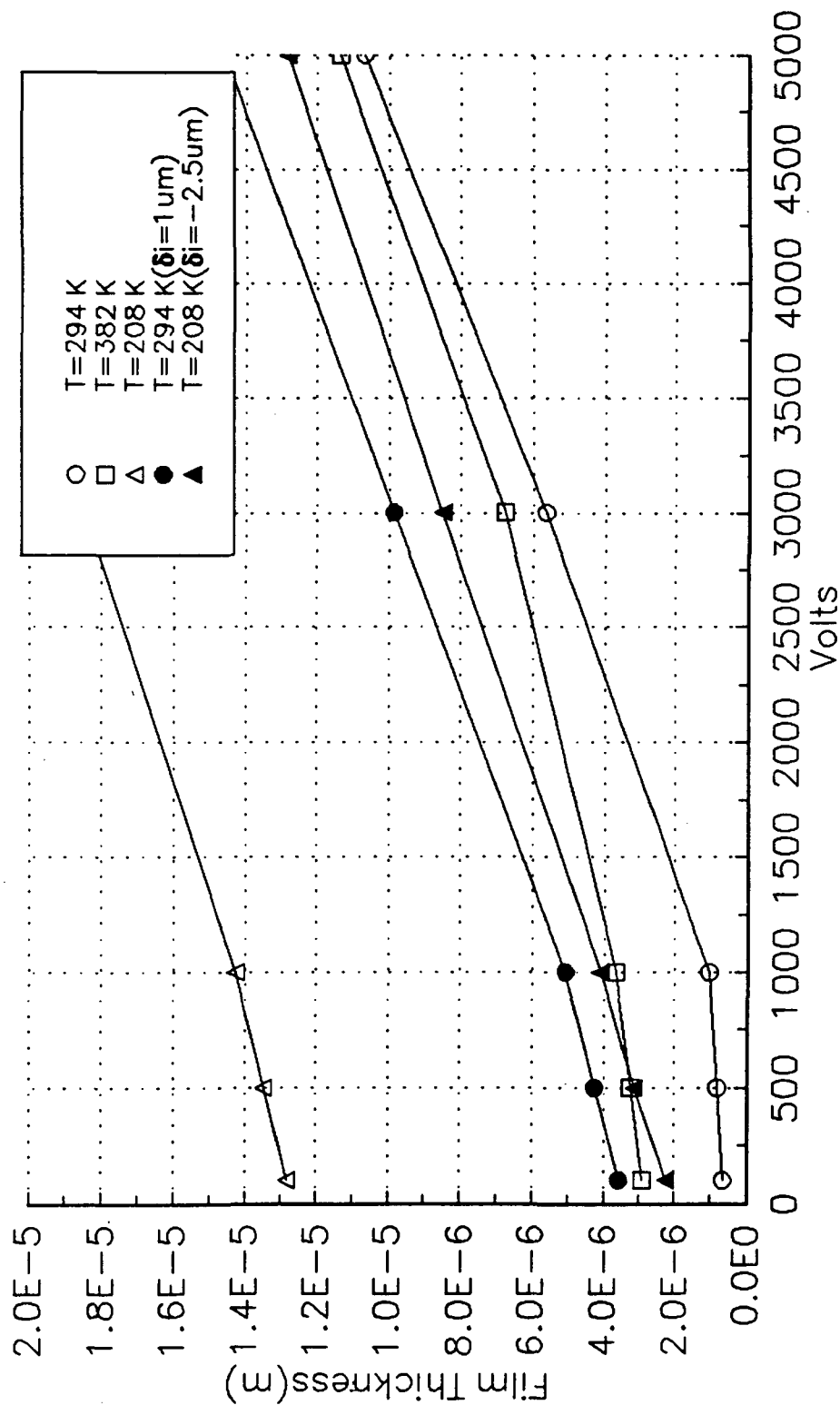### (Insulated at Outside Radius of Holder)

Figure 26. Seal Performance — Final Design

109

APPENDIX A

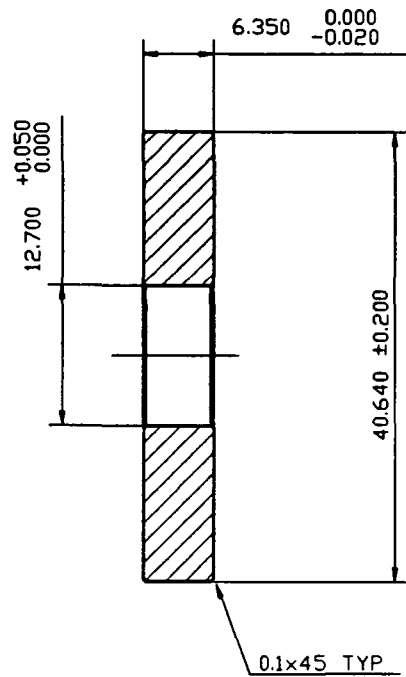## DETAILED DESIGN DRAWINGS

The detailed design drawings are presented as follows: Figure A-1 shows the assembly drawing of the seal and the test rig, Figure A-2 shows the rotor, Figure A-3 shows the seal holder, and Figure A-4 shows the deformable face assembly.

Shaft Carbon Face Rotor Piezoelectric Element Holder Housing

Bearing Wave Spring Sleeve
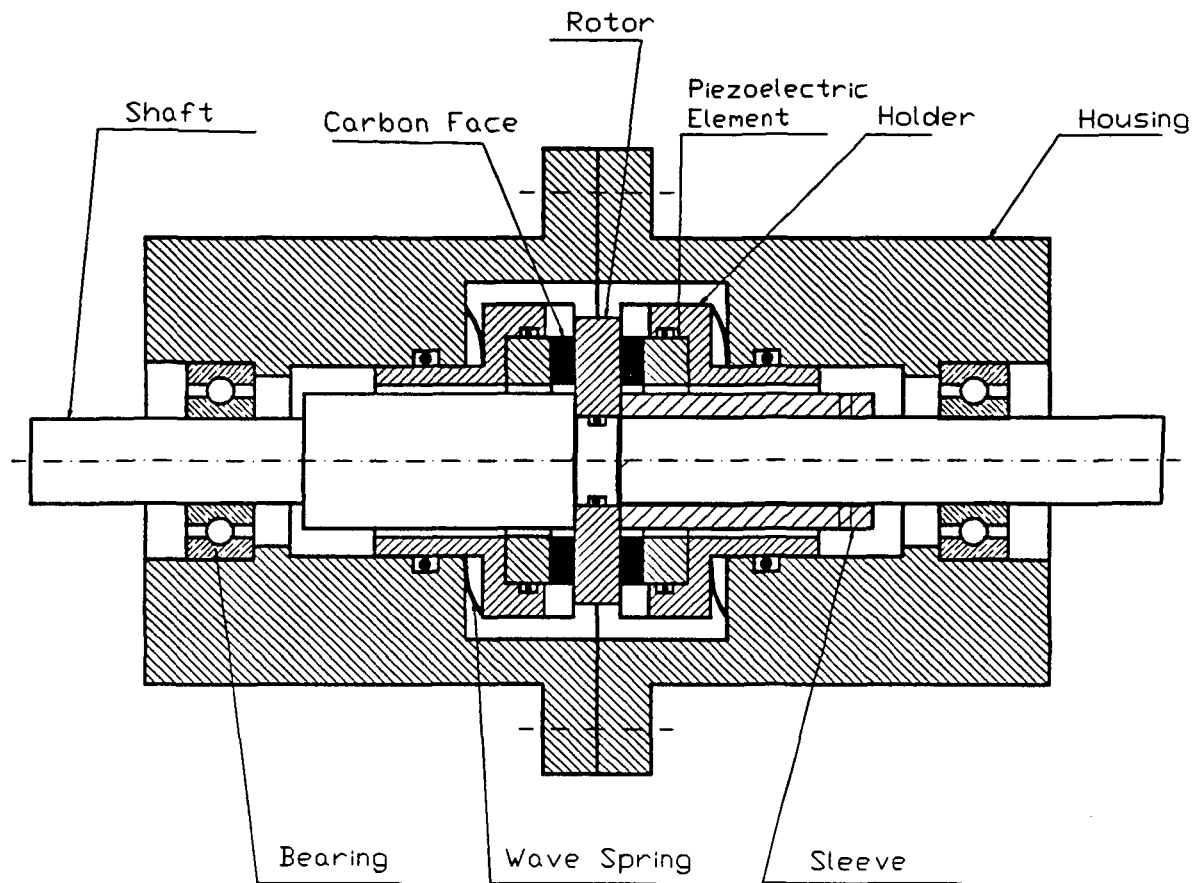
Scale 1 : 1

Figure A-1. Test Rig Assembly

6.350 $^{0.000}_{-0.020}$

12.700 $^{+0.050}_{0.000}$

40.640 ±0.200

0.1×45 TYP.
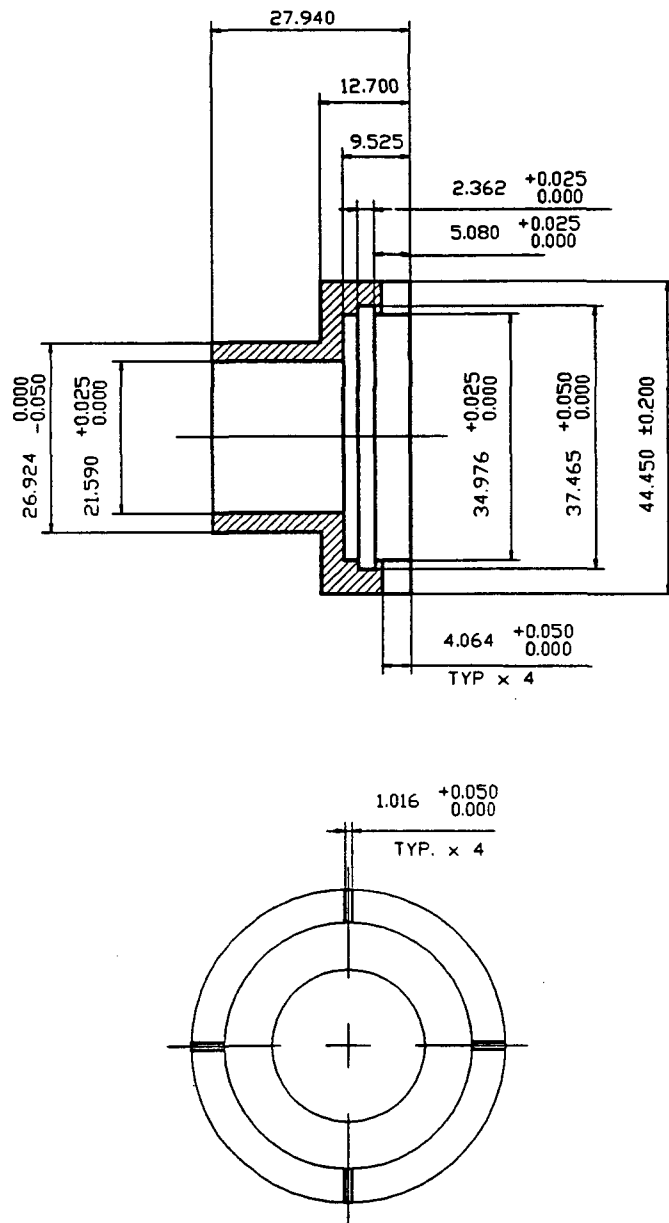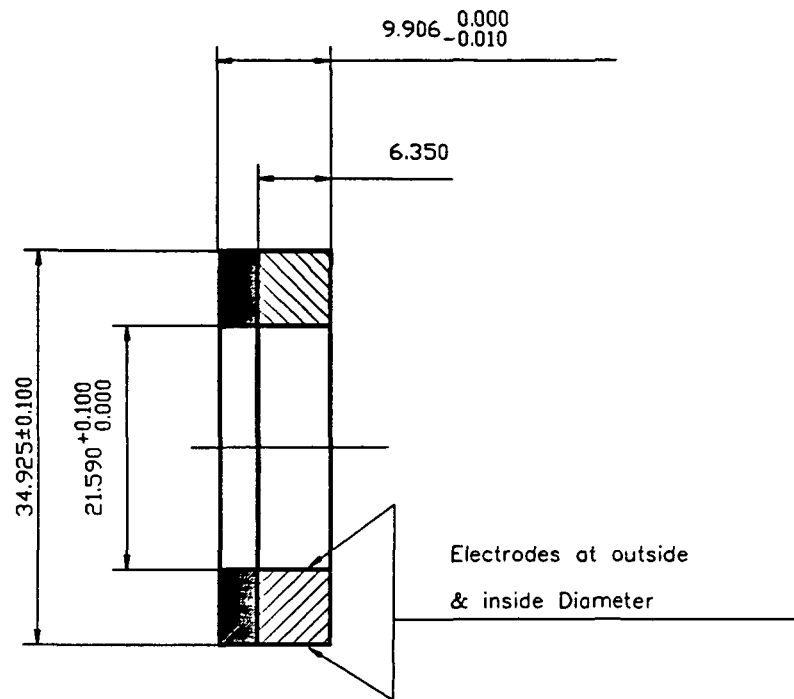
All Dimensions are in Millimeters

Scale   1.5 : 1

Figure A—2.   Rotor

All Dimensions are in Millimeters

Scale   1 : 1

Figure A—3.   Holder

$9.906^{0.000}_{-0.010}$

6.350

34.925 ± 0.100

$21.590^{+0.100}_{0.000}$

Electrodes at outside
& inside Diameter

All Dimensions are in Millimeters

Scale   1.5 : 1

Figure A—4. Deformable Face Assembly.

APPENDIX B

MATERIAL PROPERTIES

Piezoelectric Material Properties

The electromechanical constitutive relations which govern the behavior of a linear piezoelectric material are given by the following equations [Kohnke, 1989];

$$\{\tau\} = [c]\{S\} - [e]^t\{E\} \tag{43}$$

$$\{D\} = [e]\{S\} + [e]\{E\} \tag{44}$$

where

$\{\tau\}$ = 6 x 1 stress vector (N/m^2)

$\{S\}$ = 6 x 1 strain vector

$\{E\}$ = 3 x 1 electric field vector (V/m)

$\{D\}$ = 3 x 1 electric flux vector (q/m^2)

$[c]$ = 6 x 6 elasticity matrix at constant electric field (N/m^2)

$[e]$ = 3 x 6 piezoelectric matrix (stress/electric field $(N/m^2)/(v/m)$

$[\epsilon]$ = 3 x 3 dielectric matrix at constant

mechanical strain (q/(v m))

The two piezoelectric materials studied in this analysis are both transverse isotropic materials. The material matrices which govern their behavior are transversely isotropic and of the following form,

$$
[c] = \begin{bmatrix}
c_{11} & c_{12} & c_{13} & 0 & 0 & 0 \\
c_{12} & c_{11} & c_{13} & 0 & 0 & 0 \\
c_{13} & c_{13} & c_{33} & 0 & 0 & 0 \\
0 & 0 & 0 & c_{44} & 0 & 0 \\
0 & 0 & 0 & 0 & c_{55} & 0 \\
0 & 0 & 0 & 0 & 0 & c_{55}
\end{bmatrix}
\tag{45}
$$

$$
[e] = \begin{bmatrix}
0 & 0 & e_{13} \\
0 & 0 & e_{13} \\
0 & 0 & e_{33} \\
0 & 0 & 0 \\
0 & e_{25} & 0 \\
e_{25} & 0 & 0
\end{bmatrix}
\tag{46}
$$

$$[e^r] = \begin{matrix} e_{11}^r & 0 & 0 \\ 0 & e_{11}^r & 0 \\ 0 & 0 & e_{33}^r \end{matrix} \qquad [e^i] = \begin{matrix} e_{11}^i & 0 & 0 \\ 0 & e_{11}^i & 0 \\ 0 & 0 & e^{33\,i} \end{matrix} \qquad (47)$$

In the piezoelectric literature, the piezoelectric matrix is typically given as the strain/electric field at constant stress ([d] matrix). The elasticity matrix is typically presented as a compliance matrix at constant electric field ([s] m^2/N). For a transverse isotropic material, these matrices are of the following form,

$$[d] = \begin{matrix} 0 & 0 & 0 & 0 & d_{15} & 0 \\ 0 & 0 & 0 & d_{15} & 0 & 0 \\ d_{31} & d_{31} & d_{33} & 0 & 0 & 0 \end{matrix} \qquad [s] = \begin{matrix} s_{11} & s_{12} & s13 & 0 & 0 & 0 \\ s_{12} & s_{11} & s_{13} & 0 & 0 & 0 \\ s_{13} & s_{13} & s_{33} & 0 & 0 & 0 \\ 0 & 0 & 0 & s_{44} & 0 & 0 \\ 0 & 0 & 0 & 0 & s_{44} & 0 \\ 0 & 0 & 0 & 0 & 0 & s_{66} \end{matrix} \qquad (48)$$

Table 5 presents a listing of the material properties for PZT-5H and EC-98 as found in the piezoelectric commercial literature [Vernitron, EDO]. The material coefficients s_{13}, s_{44}, ϵ_{11}, and ϵ_{22} were not available at the time of this study. The s_{13} and s_{14} material coefficients are approximated from the PZT-5H coefficients as follows,

$$s_{13}(EC\text{-}98) \approx s_{13}(PZT\text{-}5H) * \frac{s_{33}(EC\text{-}98)}{s_{33}(PZT\text{-}5H)} \tag{49}$$

The dielectric coefficients, ϵ_{11} and ϵ_{22} are approximated by setting them equal to the ϵ_{33} coefficient. The errors introduced in these approximations should be negligible because the mode of deformation of concern for this study is produced primarily by the electric field. This deformation is governed by the d_{15} coefficient and is not directly affected by the coefficients which are approximated.

The imaginary part of the dielectric matrix was computed from the following relation;

$$[\epsilon^i] = -\tan\zeta\,[\epsilon^r] \tag{50}$$

where ζ is called the dissipation factor and is given in Table 5.

These properties are not in the format which is required by ANSYS, and must be transformed with the following equations [Mason, 1950],

$$[c] = [s]^{-1} \tag{51}$$

$$[e] = [d] [c] \qquad\qquad (52)$$

A coordinate transformation must also be performed to transform the material properties presented in piezoelectric literature to the format utilized in ANSYS. In the piezoelectric literature the c44 coefficient represents the shear in the yz plane, the c55 coefficient represents the shear in the xz plane, and the c66 coefficient represents the shear in the xy plane. This is not consistent with the convention used in ANSYS where the c44 coefficient represents the shear in the xy plane, the c55 coefficient represents the shear in the yz plane, and the c66 coefficient represents the shear in the xz plane. To account for these differences, the following changes are made in the elasticity and piezoelectric matrices,

$$[e] = \begin{bmatrix} 0 & 0 & 0 & 0 & e_{15} & 0 \\ 0 & 0 & 0 & e_{15} & 0 & 0 \\ e_{31} & e_{31} & e_{33} & 0 & 0 & 0 \end{bmatrix} \rightarrow [e] = \begin{bmatrix} 0 & 0 & 0 & 0 & 0 & e_{15} \\ 0 & 0 & 0 & 0 & e_{15} & 0 \\ e_{31} & e_{31} & e_{33} & 0 & 0 & 0 \end{bmatrix} \qquad (53)$$

$$[c] = \begin{bmatrix} c_{11} & c_{12} & c_{13} & 0 & 0 & 0 \\ c_{12} & c_{11} & c_{13} & 0 & 0 & 0 \\ c_{13} & c_{13} & c_{33} & 0 & 0 & 0 \\ 0 & 0 & 0 & c_{44} & 0 & 0 \\ 0 & 0 & 0 & 0 & c_{44} & 0 \\ 0 & 0 & 0 & 0 & 0 & c_{66} \end{bmatrix} \rightarrow \begin{bmatrix} c_{11} & c_{12} & c_{13} & 0 & 0 & 0 \\ c_{12} & c_{22} & c_{13} & 0 & 0 & 0 \\ c_{13} & c_{13} & c_{33} & 0 & 0 & 0 \\ 0 & 0 & 0 & c_{66} & 0 & 0 \\ 0 & 0 & 0 & 0 & c_{44} & 0 \\ 0 & 0 & 0 & 0 & 0 & c_{44} \end{bmatrix} \qquad (54)$$

Table 6 presents the properties which result when these transformations are made.

An additional property which is required for a deformation analysis is the coefficient of thermal expansion. The thermal expansion coefficient for PZT-5H is temperature dependent, given in Table 7. The thermal expansion coefficient in the direction of the poling axis is given by α_3; α_1 is the thermal expansion coefficient in the remaining two directions. These properties are not available for EC-98 and were therefore approximated by the PZT-5H thermal expansion coefficients.

For a thermal analysis, the thermal conductivities are required. The thermal conductivity for PZT-5H is listed in the piezoelectric commercial literature as 1.8 (watts/m C). This thermal conductivity was also used for the analysis of EC-98.

Material Properties for Seal Faces and Holder

The materials used for the seal faces are carbon for the stationary face and tungsten carbide for the rotor. The material used for the holder is 17-4 PH stainless steel. The properties required for a deformation analysis for isotropic materials are the elastic modulus, Poisson's Ratio and the coefficient of thermal expansion. The deformation analysis also requires the density of the rotor because of centrifugal stresses. These properties are presented in Table 8 for the seal faces and the holder.

APPENDIX C

CONVECTIVE HEAT TRANSFER COEFFICIENTS

The convective coefficients used in this mathematical model are based on a study performed by Gazley [1958]. In this study, convective coefficients of concentric cylinders were measured. These tests were performed with the inner cylinder rotating (0 -492 rad/sec), with and without axial air flow, for two gap sizes of 4.31×10^{-4} m (0.017 in) and 6.09×10^{-3} (0.24 in) at a nominal gap radius of 6.35×10^{-2} m (2.5 in).

The first step in determining the convective coefficient is to compute the Reynold's Number which is given by,

$$Re = l_G u_R / v \tag{55}$$

where l_G is the gap width, u_R is the peripheral velocity of the rotor, and v is the kinematic viscosity of the fluid. Once the Reynold's number is known, the Nusselt Number which governs heat transfer from the stator or rotor can be determined from Figures 11 or 12 in Gazley [1958], respectively. The convective coefficient can be computed from the Nusselt Number as follows,

$$H = (N_u k) / (2 l_G) \qquad\qquad (56)$$

where H is the convective coefficient, Nu is the Nusselt Number, and k is the thermal conductivity of the fluid.

An example of the procedure used to determine the convective coefficients for a stator and rotor follow, where the dimensions are based on the final seal design, presented in Appendix A. For the stator the Reynold's Number is given by,

$$Re = \frac{0.127x10^{-2}(m)\,6.97\,(m/sec)}{12.24x10^{-5}(m^2/sec)} = 72 \qquad\qquad (57)$$

where the gap width is $0.127x10^{-2}$ and the kinematic viscosity for helium at 294 K is 12.24x10-5 m^2/sec. The peripheral velocity of the shaft, based on a rotational speed of 7330 rad/sec and a radius of $0.952x10^{-3}$, is 6.97 m/sec. Based on Figure 12 in Gazley [1958], the Nusselt Number which corresponds to this Reynold's Number is 5. The convective coefficient is,

$$H = \frac{5*15.5x10^{-2}(W/mK)}{2*0.127x10^{-2}(m)} = 305\,(W/m^2K) \qquad\qquad (58)$$

where k is 15.5x10^{-2} (W/m K) for helium at 294 K.

For the rotor, the Reynold's Number is,

$$Re = \frac{0.508x10^{-2}\,(m)\,149.0\,(m/sec)}{12.24x10^{-5}\,(m^2/sec)} = 6.18x10^3 \qquad (59)$$

where the gap width between the rotor and the seal housing is 0.508x10^{-2} m. The peripheral velocity is 149.0 m/sec, based on a radius of 2.03x10^{-2} m and a rotational speed of 7330 rad/sec. From Figure 11 in Gazley [1958], the Nusselt Number is approximately 45. This results in the following convective coefficient,

$$H = \frac{45*15.5x10^{-2}\,(W/mK)}{2*0.508x10^{-2}\,(m)} = 687\,(W/m^2K) \qquad (60)$$

APPENDIX D

MODIFIED REGULA FALSI

The modified regula falsi method is a numerical procedure used to find the solution of the equation $f(x) = 0$. It is an iterative procedure which is presented graphically in Figure D-1 and given by the following algorithm [Conte, 1972]:

Given $f(x)$ continuous on $[a_0, b_0]$ and $f(a_0)*f(b_0)<0$

Set $F=f(a_0)$, $G=f(b_0)$, $w0=a0$

For $n=0,1,2,...$ until satisfied do:

    Calculate $w_{n+1}=(G*a_n-F*b_n)/(G-F)$

    if $f(a_n)*f(w_{n+1})\leq0$, set $a_{n+1}=a_n$, $b_{n+1}=w_{n+1}$, $G=f(w_{n+1})$

      if also $f(w_n)*f(w_{n+1})>0$, set $F=F/2$

    Otherwise, set $a_{n+1}=w_{n+1}$, $F=f(w_{n+1})$, $b_{n+1}=b_n$

      if also $f(w_n)*f(w_{n+1})>0$, set $G=G/2$

    Repeat until $f(w_{n+1})<$tolerance
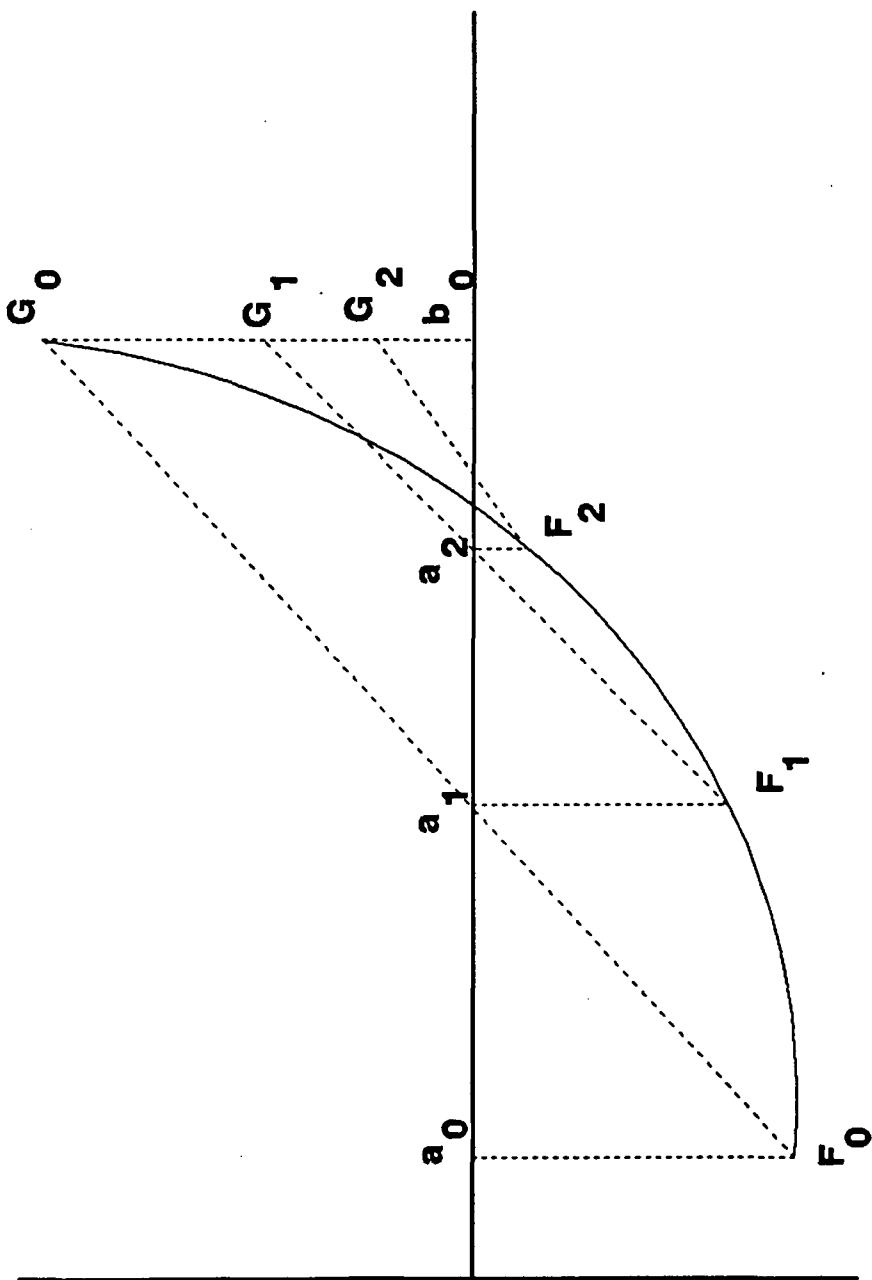
Figure D-1. Modified Regula Falsi

APPENDIX E

EXPERIMENTAL PROGRESS

The experimental evaluation of the actively controlled seal presented in this thesis is now well underway. The components of the seal (presented in Appendix A) have been machined, assembled, and preliminary tests have been completed.

The first part of the experimental study consisted of building the deformable face assembly, and measuring the coning deformation which it produced. Initial tests performed with the piezoelectric elements indicated that it was easier to electrically insulate the piezoelectric element with electrodes placed on the outside and inside radii of the piezoelectric element, and with a poling axis in the axial direction. The finite element model indicated that this modification produced essentially no change in the coning deformation. Therefore, the design of the deformable face assembly has been modified to accommodate these changes.

The carbon face of the deformable assembly is lapped and then bonded to the piezoelectric element with a conductive

epoxy. The coning of the carbon face has been measured with an optical flat illuminated by a monochromatic light source. Coning deformations as high as 2 microns have been observed with an applied voltage of 2000 volts. This agrees well with the deformation predicted by the finite element model.

The coning deformations of the deformable face assembly have also been measured with the assembly placed in the holder (presented in Figure A-3). In this configuration, it is necessary to electrically insulate the deformable face assembly from the holder which is held at 0 volts. This has been accomplished by bonding mylar with a nonconductive epoxy to the inside of the holder. The deformable face assembly also has mylar attached to the back side as well as a coating of polyurethane on the inside and outside radii. With this insulation, voltages as high as 2500 volts have been applied to the deformable face assembly without electrical breakdown.

Static pressure tests have been performed with the test rig. This involved assembling the test rig (presented in Figure A-1) and then pressurizing it to 200 psig with helium. Results from these tests indicate that the polyurethane coating on the piezoelectric element (which is nonuniform) may cause the o-ring to leak. Various nonconductive materials are currently being considered as a material for the holder. A nonconductive holder would eliminate the need for the coatings and higher manufacturing tolerances could be met.

BIBLIOGRAPHY

1. Alik, N. and Hughes, J.R., "Finite Element for Piezoelectric Vibration," _International Journal of Numerical Methods for Engineering_, No. 2, pp. 151-157, 1970.

2. Bathe, K. J., _Finite Element Procedures in Engineering Analysis_, Prentice-Hall, Inc., Englewood Cliffs, N.J., 1982.

3. Budynas, R.G., Advanced Strength and Applied Stress Analysis, McGraw-Hill, New York, New York, 1977.

4. Burcham, R.E., _Liquid Rocket Engine Turbopump Rotating Shaft Seals_, NASA SP-8121, 1978.

5. Cleaver, T.N., "Materials of Construction - Chapter 2", in _Mechanical Seal Practice for Improved Performance_, Editor Summer-Smith, J.D., Mechanical Engineering Publications Ltd. for The Institution of Mechanical Engineers, London, England, 1988.

6. Conte, S. D. and de Boor, C., _Elementary Numerical Analysis:An Algorithmic Approach_, McGraw-Hill, New York, New York, 1965.

7. Cook, R. D., _Concepts and Applications of Finite Element Analysis_, 2nd Ed., John Wiley and Sons, New York, New York, 1981.

8. DeSalvo, G.J. and Gorman, R.W., _ANSYS - Engineering Analysis System - User's Manual_, Houston, Pa., 1989.

9. Doust, T.G. and Parmar, A., "An Experimental and Theoretical Study of Pressure and Thermal Distortions in a Mechanical Seal," _ASLE Transactions_, Vol. 29, 2, pp. 151-159, 1985.

10. EDO Corporation, Western Division, "Piezoelectric Ceramics", Salt Lake City, Utah.

11. Etsion, I., Feasibility Study of a Controlled Mechanical Seal," STLE Preprint No. 90-TC-2D-1, 1990.

12. Gazley, Jr., C., "Heat-Transfer Characteristics of the Rotational and Axial Flow Between Concentric Cylinders," Transactions ASME, Vol. 80, pt. 1, 1958, pp. 79-90.

13. Kohnke, P.C., ANSYS Theoretical Manual, Swanson Analysis Systems, Inc., Houston, PA, 1989.

14. Heilala, A.J. and Kangasneimi, A., "Adjustment and Control of a Mechanical Seal Against Dry Running and Severe Wear", Proc. BHRA 11th International Conference on Fluid Sealing, Cannes, France, April 8-10, Paper H-2, 1987.

15. Hughes, W.F., Basu, P., Beatty, P.A., Beeler, R.M. and Lau, S., "Dynamics of Face and Annular Seals with Two-Phase Flow," NASA Contractor Report 4256, Prepared under Lewis Research Center Grant NAG3-166, 1989.

16. Mason, W.P., Piezoelectric Crystals and their Applications to Ultrasonics, Van Nostrand, New York, New York, 1950.

17. Mayer, E., Mechanical Seals, 3rd Ed., Newnes-Butterworth, London, England, 1977.

18. Metcalf, R., "A Fluid Mechanical Analysis of Axisymmetric Face Seals on the Basis of Constant Viscosity Laminar Flow," Report AECL-4073, Chalk River, Ontario, Atomic Energy of Canada Limited, December, 1971.

19. Metcalf, R., "End-Face Seal Deflection Effects - The Problems of Two-Component Stationary or Rotating Assemblies," ASLE Transactions, Vol. 23, 4, pp. 393-400, 1979.

20. Metcalf, R., "Effects of Pressure and Temperature Changes on End-Face Seal Performance," ASLE Preprint No. 81-LC-1A-2, 1981.

21. Nau, B. S., "Hydrodynamic Lubrication in Face Seals," Proceedings 3rd International Conference on Fluid Sealing, Paper E5, BHRA Fluid Engineering, Cranfield, 1967.

22. Salant, R.F., Miller, A.L., Kay, P.L., Kozlowski, J., Key, W.E. and Algrain, M.L., "Development of an Electronically Controlled Mechanical Seal," _Proceedings 11th International Conference on Fluid Sealing_, Paper H3, BHRA Fluid Engineering, Cranfield, 1987.

23. Salant, R.F. and Key, W.E., "Development of an Analytical Model for use in Mechanical Seal Design," _Proceedings 10th International Conference on Fluid Sealing_, Paper G3, BHRA Fluid Engineering, Cranfield, 1984.

24. Salant, R.F., Giles, O. and Key, W.E., "Design of Controllable Mechanical Seals," _Tribological Design of Machine Elements_, Elsevier Science Publishers B.V., Amsterdam, 1989.

25. Sobin, A.J. and Bissell, W.R., _Turbopump Systems for Liquid Rocket Engines_, NASA SP-8107, 1974.

26. Vernitron Piezoelectric Division, "Piezoelectric Technology Data for Designers," Bedford, Ohio.

27. Zuk, J., "Fundamentals of Fluid Sealing," NASA Technical Report, Lewis Research Center, Cleveland, OH., 1973.